Fabrication and Characterization of Optical Microfibers

Filipe Miguel Moreira Marques
Mestrado Integrado em Engenharia Física
Departamento de Física e Astronomia
2019

Orientador
Orlando José dos Reis Frazão, Professor Auxiliar Convidado, Faculdade de Ciências

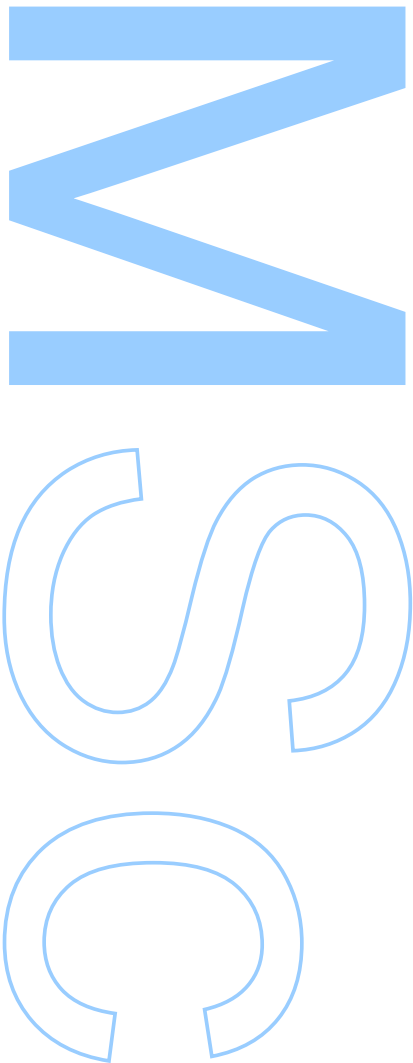

U.PORTO

FACULDADE DE CIÊNCIAS
UNIVERSIDADE DO PORTO

Todas as correções determinadas pelo júri, e só essas, foram efetuadas.

O Presidente do Júri,

Porto, _____/_____/_____

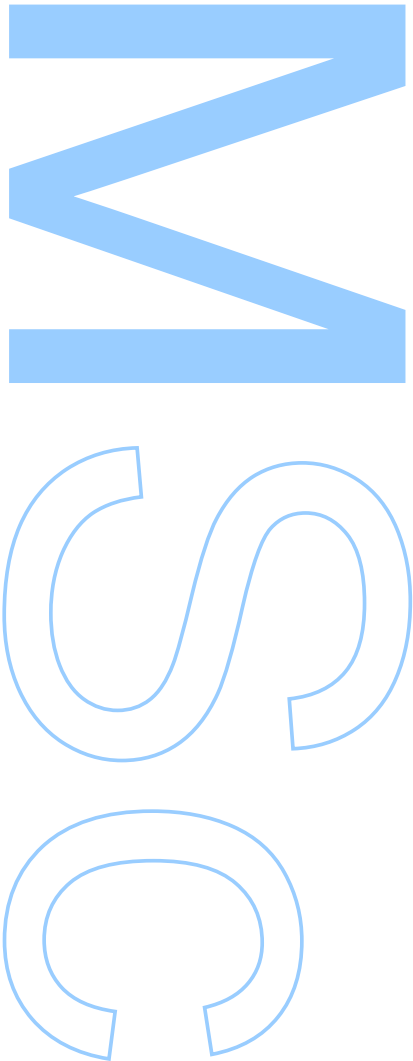

UNIVERSIDADE DO PORTO

MASTERS THESIS

Fabrication and Characterization of Optical Microfibers

Author:
Filipe MARQUES

Supervisor:
Orlando FRAZÃO

A thesis submitted in fulfilment of the requirements
for the degree of MSc. Engineering Physics

at the

Faculdade de Ciências da Universidade do Porto
Departamento de Física e Astronomia

November, 2019

" The most important step a man can take. It's not the first one, is it?
It's the next one. Always the next step, Dalinar. "

Brandon Sanderson, Oathbringer

Acknowledgements

This dissertation is a milestone in my personal and academic path, but by no means was it accomplished individually. I would like to express my unending gratitude to all who have helped me along the way.

First, and always, I would like to thank my family. To my parents, João and Isabel, thank you for all the sacrifices, support and love, and to my siblings, Diogo, Gonçalo and Raquel, for putting up with a guy with too much information in his head and a tendency to talk nonsense. I would also like to thank my cousin Inês for all the support during this work.

To my supervisor, Dr. Orlando Frazão, for proposing such an interesting and challenging project, and guiding me all the way while letting me follow my ideas. Your knowledge, patience and encouragement were a driving force behind this work.

To my mentors and colleagues at the Center of Applied Photonics, INESC-TEC, for welcoming me and providing the means, expertise and support for the conclusion of this work. I would like to specifically acknowledge Catarina Monteiro, Paulo Robalinho, Paulo Santos, Dr. Susana Silva and Dr. Paulo Marques for all the assistance, guidance and encouragement.

I would like to acknowledge the FCT – Fundação para a Ciência e a Tecnologia – within the project project "Ultragraf - Harnessing third-harmonic generation in graphene-coated optics - new devices for ultrafast pulse measurement and frequency upconversion", (M-ERA-NET2/0002/2016), which funded a vital part of this work.

To finalize, this dissertation may mark the end of an academic cycle, but my life is defined by every single contact and experience I've had up to this point. I would like to thank every single family member, friend, colleague, acquaintance, teacher, coach, athlete, and so on... You have made me who I am today, and I thank you from the bottom of my heart.

UNIVERSIDADE DO PORTO

Abstract

Faculdade de Ciências da Universidade do Porto
Departamento de Física e Astronomia

MSc. Engineering Physics

Fabrication and Characterization of Optical Microfibers

by Filipe MARQUES

Optical fiber sensing has evolved into one of the most fruitful and promising fields of applied physics. Ever since the 1960s, with the invention of the laser and consequent technological advances, optical fibers have been developed into numerous applications.

When the diameter of an optical fiber is of the order of the wavelength of propagating light some extraordinary properties arise, including large evanescent fields, strong confinement, and controllable dispersion. Thus, these so-called optical microfibers are promising structures in fields such as optical sensing, particle manipulation, and nonlinear applications. This dissertation explores the fabrication and characterization of optical microfibers.

An extensive review of the literature on the subject is given, followed by some theoretical concepts regarding light propagation in microfibers and the fabrication of microfibers by *heat-and-pull*. The apparatus and sequence for the fabrication of microfibers, using an electric microheater and symmetrical pulling stages, is detailed.

The characterization of the microfibers is divided into three sections. Firstly, a geometric profiling is performed: a simple, contactless method for the measurement of the microfibers' diameter is developed and the results are compared to the theoretical model. Afterward, the optical transmission, both in the infrared and visible range, is monitored during the fabrication process: the loss of the microfibers is related to the pulling speed, and a method based on modal dissipatioin for the real-time measurement of the diameter of the microfibers is proposed. At last, the optical response of the microfibers to external physical parameters, such as temperature and strain, is analyzed. In the end, some possible paths for further investigation are presented.

Keywords: optical microfibers, electric microheater, optical fiber sensors

UNIVERSIDADE DO PORTO

Resumo

Faculdade de Ciências da Universidade do Porto
Departamento de Física e Astronomia

Mestrado Integrado em Engenharia Física

Fabricação e Caracterização de Microfibras Óticas

por Filipe MARQUES

As propriedades e potencialidades das fibras óticas tornaram o desenvolvimento de sensores em fibra um dos campos mais promissores da física aplicada. Desde a década de 60, com a invenção do laser e os avanços tecnológicos que se seguiram, as fibras óticas foram inseridas em múltiplas aplicações.

Quando o diâmetro de uma fibra ótica é da ordem de grandeza do comprimento de onda da radiação propagante surgem propriedades óticas extraordinárias, como campos evanescentes extensos, forte confinamento e dispersão controlável. Assim sendo, as microfibras óticas apresentam-se como estruturas promissoras nos campos de deteção ótica, manipulação de partículas e aplicações não-lineares. Esta dissertação explora a fabricação e caracterização de microfibras óticas.

Inicialmente, é feita uma revisão extensiva da literatura publicada sobre o tema. Seguem-se alguns conceitos teóricos quanto à propagação de luz em microfibras, e a fabricação de microfibras por métodos de estiramento. De seguida, o sistema e técnica experimental de fabricação das microfibras, por estiramento de fibras óticas standard aquecidas com um microforno elétrico, é detalhado. A caracterização das estruturas fabricadas é dividida em três partes. Em primeiro lugar procede-se a um perfilamento geométrico: é desenvolvido um método simples e sem-contacto para a medição do diâmetro das microfibras, e os resultados são comparados com um modelo teórico. De seguida, procede-se à análise da evolução da transmissão ótica, nas gamas do infravermelho próximo e visível, durante o processo de fabricação. Relaciona-se a qualidade das microfibras com a velocidade de estiramento, e desenvolve-se uma técnica para a medição em tempo real do diâmetro das

microfibras, por dissipação de modos óticos. Por fim, analisa-se a resposta das microfibras a parâmetros físicos externos, como a temperatura e o estiramento (*strain*). No final, algumas hipóteses de trabalho futuro são apresentadas.

Palavras-chave: microfibras óticas, microforno elétrico, sensores em fibra ótica

Contents

List of Figures

List of Tables

Chapter 1

Introduction

1.1 Motivation

Light and its related natural phenomena, such as shadows, reflections and rainbows, have captivated the minds of History's greatest thinkers for millennia. From the theories of light and vision of Aristotle, Euclid, and Archimedes in Ancient Greece, to Newton's corpuscular theory, Maxwell's Equations for the electromagnetic theory and, more recently, the field of quantum electrodynamics, with contributions from Heisenberg, Pauli and Feynmann, among others, the study of light, *Optics*, has come a long way.

Experimentally, the field of Optics experienced an increase in productivity with the invention of the laser, in 1960, by Theodore H. Maiman. In particular, the laser and related technological advances led to the optimization of the optical fiber.

An Optical Fiber is a cylindrical dielectric waveguide that transmits light along its axis. It is composed of two layers: the core—the inner layer—and the cladding—the outer layer, with a lower refractive index—, usually made from doped fused silica. Due to its characteristics, such as small footprint, high flexibility, durability under harsh conditions and immunity to electromagnetic interference, optical fibers have been widely adopted for telecommunications and sensing applications.

In recent years, the reach for the nanoscale has led to the development of optical microfibers. Optical microfibers are waveguides, mostly fabricated from standard optical fibers, with diameters of the same order of magnitude as the wavelength of guided light. In 2003, Tong *et al.* [1] published the first successful report of subwavelength diameter silica wires with low-loss and great diameter uniformities, and, since then, the field has grown tremendously. Optical microfibers display an array of interesting properties such

as large evanescent fields or strong confinement, excellent surface smoothness, great robustness and extraordinary mechanical flexibility, making them suitable for applications in nonlinear optics, particle manipulation, and sensing [2]. Furthermore, due to their cylindrical geometry, microfibers are also far simpler structures than other microstructurized waveguides in terms of fabrication, optical characterization and theoretical modeling [3].

1.2 Aims and Objectives

The main objective of this work is the development and optimization of a tapering rig for the fabrication of microfibers, and consequent characterization of the produced structures.

The following objectives were established:

- Assembling and optimizing a functional apparatus for the fabrication of microfibers through heat-and-pull using an electric microheater.
- Fabricating multiple microfibers, with a particular focus on microfibers with diameters lower than 10 μm.
- Characterizing the produced microfibers, not only for the optimization of the tapering setup, but also for sensing applications.

1.3 Structure

This dissertation is divided into nine chapters, of which three aim to introduce the theme with a literature review and the underlying theoretical background, while four are relative to the experimental work developed during this project.

In this first chapter, the motivation and main goals for this work are defined. A delineation of the document is presented and resulting outputs are listed.

Chapter 2 contains a review of the state of the art regarding optical microfibers, including a brief historical overview, the main fabrication methods and typical applications, based on the preeminent publications on the subject.

Chapter 3 gives a theoretical exposition of the main optical properties of microwires, based on the electromagnetic theory, and focusing on modal propagation, power distribution and confinement of the fundamental mode; nonlinear effects and dispersion in microwires are also introduced.

Chapter 4 continues the theoretical background with the analysis of a simple heat-and-pull model for the shape of microfibers and a discussion of light propagation in the transition regions of a microfiber.

In Chapter 5, the depiction of the experimental work begins, with the description of the tapering rig and detailing of the fabrication process.

Chapter 6 presents the characterization of the microfiber shape, and its relation to the fabrication parameters. A contactless technique for the profiling of microfibers is presented and the data is compared to the theoretical model.

The characterization of the optical transmission during the fabrication process is performed in Chapter 7. The ideal fabrication parameters, concerning the final loss, are discussed. A method for the precise measurement of the microfiber's waist diameter based on modal dissipation is proposed.

Chapter 8 explores some applications of the microfibers as fabricated. The optical response of the microfibers to temperature, both in air and in water, and to strain is analyzed.

Chapter 9 concludes the work, with a summary of the main developments and a discussion of possible improvements.

1.4 Outputs

Filipe Marques, Orlando Frazão, *Nanofiber Diametre Control by Mode Dissipation*, 4as Jornadas em Engenharia Física, Física, Física Médica e Astronomia 2019.

Filipe Marques, Orlando Frazão, *Transmission Properties of Optical Fibers during Taper Fabrication: Adiabaticity, Mode Dissipation, and Diameter Control*, 3rd Doctoral Congress in Engineering — DCE2019 .

Chapter 2

State of the Art

Optical Microfibers are optical fibers with diameters comparable to, or thinner than, the wavelength of the light propagating in them. Thus, they are often of the order of 10 μm or smaller. In literature, and depending on the diameter, these structures are also referred to as "optical nanofibers", "subwavelength waveguides", "optical fiber nanowires and microwires", "optical fiber nanotapers", "ultrathin fibers" and others.

Despite being a relatively recent subject, there is a rather diverse amount of literature already published, ranging from the theoretical analysis of microfibers' properties to their fabrication and characterization techniques, and primary applications. This vows for the interest and practical utility of these structures. There are even some quite comprehensive review articles worth noting in references [3–6].

In this chapter, the most widespread fabrication and characterization techniques for optical micro/nanofibers will be presented, followed by an extensive analysis of typical and potential applications, as reported in literature.

2.1 Fabrication of Optical Microfibers

The history of microfibers dates back to the end of the 20^{th} century, when some attempts were made at the fabrication of thin amorphous wires of materials such as silica, silicon, and boron, mainly by bottom-up processes [7]. However, their impact was reduced due to high diameter inhomogeneities along the length, which resulted in extremely elevated transmission losses. It was only in 2003, when Tong *et al.* [1] demonstrated low loss optical waveguiding in wires with diameters far below the wavelength of guiding light through a top-down method, that this research topic truly gained momentum.

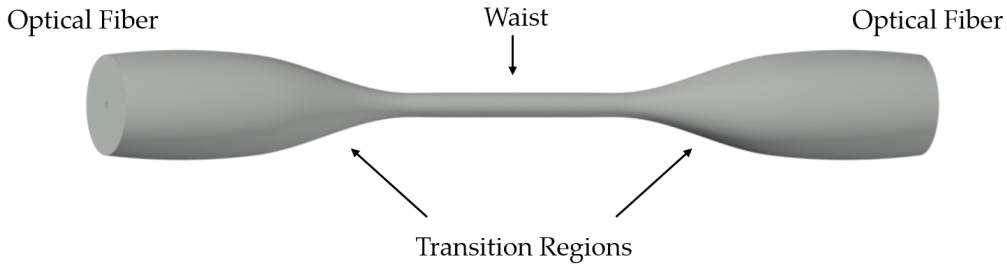

FIGURE 2.1: Schematic of a general taper profile, depicting the untapered, transition, and waist regions.

Since then, investigation groups kept their focus on top-down methods (that is, by reducing the size of macroscopic samples, such as Standard Telecom Fibers). Here, the clear majority rely on the mass conservation of heat-and-pull techniques, where a fiber is heated to its softening point while being stretched longitudinally. This decreases the fiber's diameter, creating a narrow filament—the waist—connected to the unstretched fiber by transition regions, as depicted in Figure 2.1. A simple analysis of geometry of these structures—the tapers— can be found in T. A. Birks and Y. W. Li's 1992 work: *"The Shape of Fiber Tapers"* [8]. It is shown that the shape of a microfiber can be predicted considering the fabrication parameters (a further analysis will be provided in Chapter 4).

Heat-and-pull techniques can be divided into the following subcategories: (A) Self-Modulated Taper Drawing; (B) Flame Brushing and (C) Modified Flame Brushing.

2.1.1 Self Modulated Taper Drawing

The Self Modulated Taper Drawing technique was reported by Tong *et al.* in 2003 [1] and is generally credited as the prompt for the renewed interest to the optical micro/nanofiber field. Despite having fallen into disuse, it is still worthy of analysis, at least for historical reasons.

This method consists on a two-step process: firstly, the flame brushing technique is used to create a micrometer-diameter wire that is broken into two at its waist; then, one of them is wrapped onto a small sapphire tip heated by flame. This sapphire tip, with a diameter of about 80 μm absorbs the flame's thermal energy and confines the heating to a small volume, allowing for the further drawing of the fiber to submicron diameters by precisely calibrated stages (Figure 2.2).

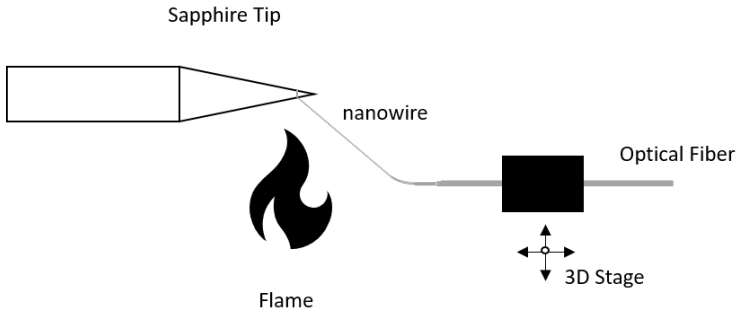

FIGURE 2.2: Self Modulated Taper Drawing technique. (Diagram based on reference [1])

The Self Modulated Taper Drawing was used to fabricate silica wires with diameters down to 20 nm with lengths of tens of millimeters and diameter uniformities of about 10^{-5} [9]. Losses below 0.1 dBmm^{-1} were achieved for wires with diameters greater than 430 nm and 1100 nm, at 630-nm and 1550-nm wavelength, respectively [1].

A downside of this method is that it produces wires with only one end pigtailed—connected to the untapered fiber—, which brings connectivity issues when considering integration in common fiber optics devices.

2.1.2 Flame Brushing

The Flame Brushing technique is probably the most widely adopted method for microfiber fabrication. It relies on a traveling millimeter-sized flame as the heating source that softens the fiber while computer-controlled translation stages stretch it. Usual setups employ butane [10], hydrogen [11, 12], oxygen, or combinations of these gases [13–16], burning at temperatures in the 1400-1700 °C range, close to fused silica's melting point, of about 1700–1730 °C [17].

Early reports of microfiber fabrication by flame brushing have shown wires with radii as small as 30 nm, over lengths of hundreds of millimeters [18]. Brambilla *et al.* have shown the reproducibility of this method, producing several identical wires with radii of 375 nm with average losses of 0.0204 dB/mm at 1.300 μm wavelength [13]. In 2017, a report demonstrated reasonable control of the diameter to within 5 nm of expected waist dimensions ranging from 800 nm to 1300 nm [12]. Some other groups have implemented setups for the precise control of taper profiles, and especially the transition regions, based on numerical models for the flame path during pulling [11, 14, 15].

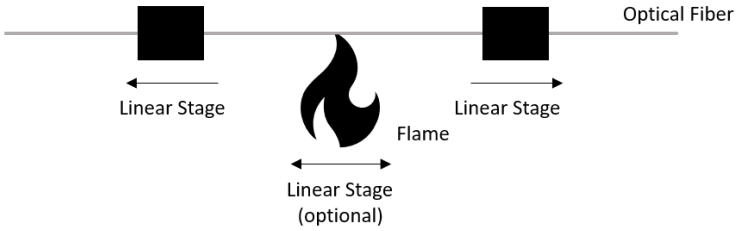

FIGURE 2.3: Schematic of a simple Flame Brushing apparatus.

In the Flame Brushing Technique, as the microfiber is produced from the tapering of standard optical fibers, it has both ends pigtailed. Its integration in common fiber optics structures and devices is immediate.

The main downsides of the Flame Brushing technique are that the fabricated microfibers show elevated OH content, as result of water vapor during gas combustion, and that the surface roughness is heavily affected by flame turbulence.

2.1.3 Modified Flame Brushing

The Modified Flame Brushing technique is similar to the Flame Brushing, the only difference being the heat source. In this case, the flame is replaced by a microheater [19–27] or a CO2 laser beam [28–31].

2.1.3.1 Microheater

A microheater is a resistive element whose temperature can be adjusted based on the current flowing through it. This level of temperature control allows the manufacture of microfibers from low softening-temperature glasses, such as compound silicate glasses, and, being a stable heat source, also decreases the defects caused by flame turbulence of the flame brushing technique [22]. Microfibers produced this way also show an extremely low OH content.

In 2005, Brambilla *et al.* manufactured long microfibers (up to 100 mm) with diameters down to 90 nm from lead-silicate and bismuth-silicate glasses with losses of a fraction of dB/mm at 1.55 μm [22]. Other groups have presented similar values [19, 32]. There have been attempts at producing microfibers with lengths up to 1 m [21, 27].

2.1.3.2 CO2 laser

Contrary to the flame and microheater cases where the process involves the heating of the surface of the fiber, heating with a laser beam involves the fiber absorbing radiation and heating from the inside. Thus, there is an inverse square relation between fiber radius and heating for a CO2 laser source that limits the minimum waist diameter for a given CO2 laser power. As is, there have been reports of low-loss tapers with diameters down to 3–6 μm [28–30]. Hartung *et al.* proposed an indirect method where the laser beam is used to heat a micro-furnace [31].

2.1.4 Other Techniques

There have also been reports on microfiber fabrication by etching [33, 34] and direct drawing from bulk [35, 36]. The former relies on the physical removal of material from the surface of a fiber using acids, namely the hydrofluoric acid, and generally provides samples with poor surface roughness and therefore high propagation loss. The later works by pulling wires straight from a bulk: a heated rod is brought into contact to the material where, by taking the rod away, a filament is formed. It is used when the desired material is unavailable in fiber form. However, the fibers fabricated this way present poor diameter uniformity and lack core/cladding structure.

2.2 Optical Microfiber-Based Applications

Optical microfibers have been used in a wide range of applications (please refer, for example, to reference [37] for an extensive overview). In particular, there have been reports of microfiber-based *i*) Optical Sensing; *ii*) Optical Manipulation; and *iii*) Nonlinear Applications.

2.2.1 Optical Sensing

For waist diameters of the order of magnitude of the guided light's wavelength, a considerable portion of the optical power resides on the evanescent field outside the fiber's physical boundaries, overlapping with the surrounding environment (for a detailed explanation, refer to Chapter 3). Changes in the environment result in changes in the output of the device, allowing microfibers to be used as sensors.

So far, there have been reports of temperature [38–43], electrical current [44–47], humidity [48, 49], refractive index [50–54], force [55, 56], magnetic field [57–59], acoustic [60, 61] and gas [62–64] sensors.

Optical sensing can occur either through the intensity, phase, or spectral profile of the transmitted/reflected light, and is generally accomplished through some common architectures, as illustrated in Figure 2.4, including:

- Straight microfiber [39, 54, 56];
- Microtip. Cleaving a microfiber at the waist makes it possible to probe and interrogate extremely small volumes due to the radiation that it is back scattered [53, 65];
- Microfiber with a fiber Bragg Grating, a periodic perturbation on the tapered fiber, either achieved by etch erosion, focused ion beam milling or femtosecond laser irradiation [38, 66];
- Mach-Zehnder interferometer made of two strands of microwires [67];
- Microfiber Coupler, made by tapering two optical fibers simultaneously [42, 43, 55, 57, 59]; and Coupler Tip [68];

By assembling the microfiber into a ring-like structure, a resonator can be formed by evanescent coupling at the overlapping area. The most used geometries are (a) loop [69, 70]; (b) knot [40, 71] and (c) coil [46, 47, 51, 52].

Optical microfibers can also be functionalized, usually for biologic applications [72], with materials such as nanoparticles [63], graphene layers [64] and other surface coatings [48, 62].

(A) Straight Microfiber

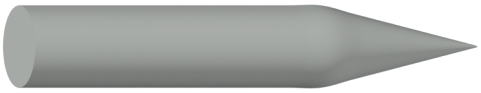

(B) Microtip Sensor

(C) Microfiber with Bragg Grating

(D) Mach-Zehnder Interferometer

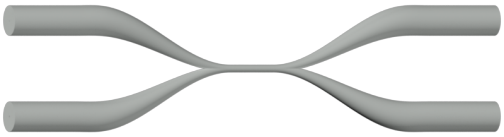

(E) Microfiber Coupler

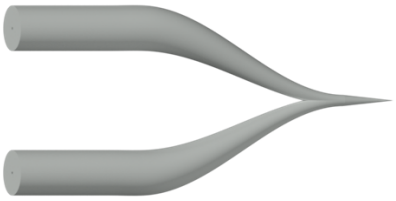

(F) Microfiber Coupler Tip

(G) Loop

(H) Knot

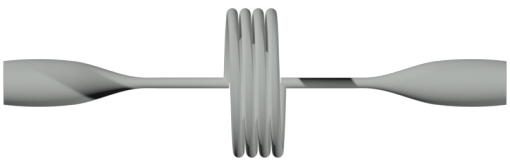

(I) Coil

FIGURE 2.4: Common microfiber-based sensor architectures. Based on the division proposed by Chen *et al.* [73].

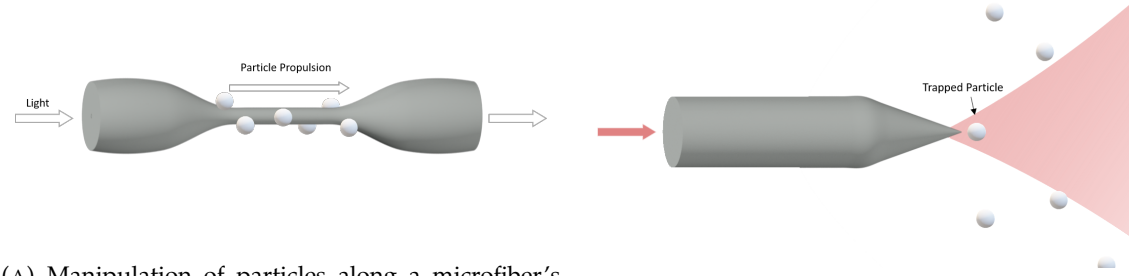

(A) Manipulation of particles along a microfiber's waist

(B) Microfiber Optical Tweezers

FIGURE 2.5: Schematic diagrams of Microfiber-based Optical Manipulation

2.2.2 Optical Manipulation

If the evanescent field at the taper's waist is large, it can be used to manipulate particles (Figure 2.5a). The particles are: (a) attracted to the high-intensity region by the gradient force and (b) propelled along the direction of propagation of light by the radiation pressure. This has been predicted to occur when the optical microfiber's diameter is about two times smaller than the wavelength of propagating light [74]. This technique has been used to propel polystyrene particles [75] and Cs atoms [76] (the later using two counter-propagating beams). Maimati *et al.* have demonstrated a system for trapping and propelling dielectric particles based on the excitation of higher-order modes at the fiber waist [77].

Similarly, optical trapping and manipulation of particles may occur using microfiber tips, as in Figure 2.5b. As the propagating beam rapidly diverges, leaving the waveguide, it creates high gradients on the intensity profile that can be used to trap microscopic particles at the region of maximum intensity. When compared to usual optical tweezers setups the use of microfibers decreases the power needed for trapping and allows for small probe dimensions and sub-micrometric spot sizes [78]. Microparticle and cell 3D-patterning has been accomplished [79].

These methods provide new ways for biophotonic and biological researches with particles and cells in a highly organized manner.

2.2.3 Nonlinear Applications

When the waist diameter of the optical fiber is about half the wavelength, the evanescent field is highly reduced, and the propagating mode is confined inside the fiber's volume, leading to high optical intensities (see Chapter 3). This, combined with the dispersion

characteristics of optical microfibers, makes them very useful for low threshold nonlinear applications, such as Harmonic and Supercontinuum generation, and Pulse Compression.

Third Harmonic Generation ($\omega \rightarrow 3\omega$) has been successfully demonstrated in silica microfibers on the ultraviolet (UV) and infrared (IR) ranges [80–82]. Manipulating the taper profile allows for the generation of broadband 3ω radiation [83]. Resonance architectures have been proposed as a method for increasing the conversion efficiency [84, 85]. Despite $\chi^2 = 0$ in bulk glass, in the nano-domain there is a contribution of surface dipoles on the glass/air interface [86]. The field strength at this interface and the microwire volume allow for the generation of Second Harmonic $(\omega \rightarrow 2\omega)$. This has already been experimentally detected but not fully optimized since the experiments were focused on third Harmonic [81, 87].

Low threshold supercontinuum has been successfully generated in optical microfibers from femtosecond [88, 89] and nanosecond [90] input pulses. On asymmetrical-profile microfibers, the output spectrum was shown to be dependent on the direction of propagation [91].

Pulse Compression, possible due to the temporal periodicity of high order solitons [92], has also been obtained. Foster *et al.* reported sub-nJ compression of optical pulses from 70 fs to 6.8 fs [93].

2.3 Microfiber Limitations

The extraordinary properties of optical microfibers make them extremely useful in a wide range of applications. However, some major limitations of microfibers still need to be optimized. In particular, the fact that unprotected microfibers degrade quickly [32], and that, due to the extremely small size, microfibers are fragile [94]. Embedding and coating microfibers in materials with low refractive indexes have been studied as a solution to these concerns [95, 96].

2.4 Concluding Remarks

This Chapter examined the extensive literature published in the field of optical microfibers and nanofibers. This field has had a tremendous growth since Tong's 2003 paper [1].

There are many ways to fabricate microfibers, however, the most widely adopted techniques resort to the mass conservation of *heat-and-pull* techniques, either using a flame or an electric microheater as heat source. There have been reports of nanofibers with waist diameters down to 20 nm and great uniformities. Some attempts to produce long microfibers have also been made.

Optical microfibers can be used in a wide range of applications, from optical sensing of physical quantities (as temperature, refractive index, strain, and others) and biological markers, to particle manipulation and even low-threshold nonlinear effects.

Some mechanical limitations of optical microfibers still need to be addressed.

Chapter 3

Light Propagation in Optical Microwires

The theoretical analysis of light propagation in optical microfibers is of the utmost importance. Both modal propagation and dispersion are size-dependent properties. Thus, by controlling its geometry, it is possible to tailor a microfiber to specific applications.

The theoretical analysis of the optical properties of microfibers is usually performed by considering the microfiber as two distinct structures: the microwire—the constant diameter waist— and the transition regions. This Chapter will address the general optical properties of microwires[1].

3.1 Modal Propagation on Optical Microwires

The study of optical microwires arises from neglecting the transition regions of a microfiber. Considering the high index contrast between the glass and the surrounding environment (~ 0.5), and the micrometric cross-section, the small index contrast that may remain from the preform's core (~ 0.05) may be ignored. It is reasonable to assume a circular cross-section of radius a (diameter $d = 2a$) and index n_1 and an infinite cladding of index n_2. The step-index profile of the waveguiding system along the radial direction, r, is (Figure 3.1):

$$n(r) = \begin{cases} n_1, & 0 < r < a \\ n_2, & r \geq a \end{cases} \tag{3.1}$$

[1] An extensive analysis of these properties can be seen in Limin Tong and Michael Sumetsky's book *"Subwavelength and Nanometer Diameter Optical Fibers"* [97].

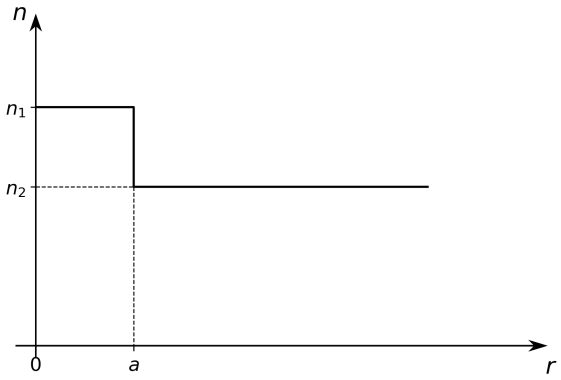

FIGURE 3.1: Index profile of an optical microwire.

Considering a non-dissipative and source-free wire, it is possible to reduce Maxwell's equations to the Helmholtz equations [98]:

$$\begin{aligned}\left(\nabla^2 + n^2k_0^2 - \beta^2\right)\vec{E} = 0\\ \left(\nabla^2 + n^2k_0^2 - \beta^2\right)\vec{H} = 0\end{aligned} \tag{3.2}$$

where ∇^2 is the *Laplacian*, $k_0 = 2\pi/\lambda$ the wave number, λ the light wavelength in vacuum, and β is the propagation constant. $\vec{E}$ and $\vec{H}$ are the electric and magnetic fields, respectively.

In cylindrical coordinates, Eqs. 3.2 can be analytically solved with eigenvalue equations for various modes [99]:

—for Hybrid Modes, HE_{vm} and EH_{vm}:

$$\left\{\frac{J_v'(U)}{UJ_v(U)} + \frac{K_v'(W)}{WK_v(W)}\right\}\left\{\frac{J_v'(U)}{UJ_v(U)} + \frac{n_2^2K_v'(W)}{n_1^2WK_v(W)}\right\} = \left(\frac{v\beta}{k_0n_1}\right)^2\left(\frac{V}{UW}\right)^4 \tag{3.3}$$

—for TE_{0m} modes:

$$\frac{J_1(U)}{UJ_0(U)} + \frac{K_1(W)}{WK_0(W)} = 0 \tag{3.4}$$

—for TM_{0m} modes:

$$\frac{n_1^2J_1(U)}{UJ_0(U)} + \frac{n_2^2K_1(W)}{WK_0(W)} = 0 \tag{3.5}$$

where J_v is the vth-order Bessel function of the first kind, K_v is the vth-order modified Bessel function of the second kind. In Eq. 3.3, the prime symbol ($\prime$) denotes the first derivative of the function.

The parameters U and W are related to the light propagation constant in vacuum (k_0) and in the waveguide (β), by:

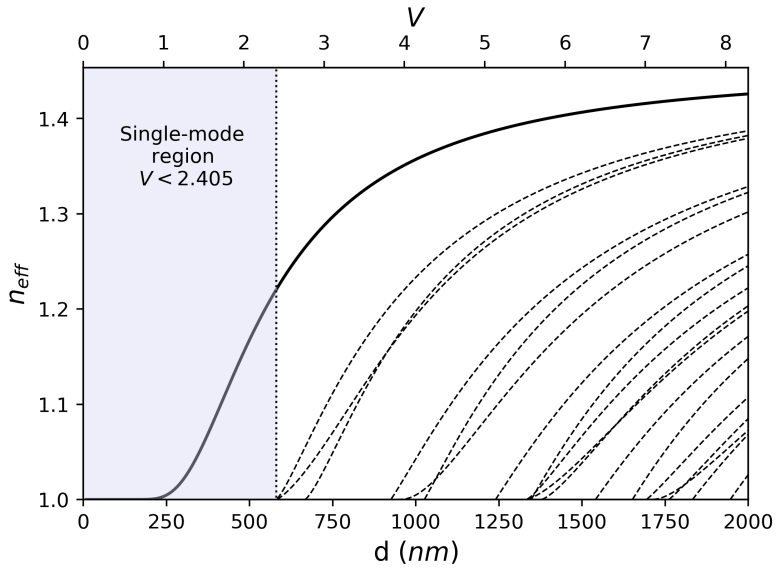

FIGURE 3.2: Modal propagation dependence on the diameter (bottom axis) and V-number (top axis) for silica wire, on air. (Simulations performed at 800 nm wavelength)

$$U = a\sqrt{k_0^2 n_1^2 - \beta^2} \tag{3.6}$$

$$W = a\sqrt{\beta^2 - k_0^2 n_2^2} \tag{3.7}$$

The V number, an dimensionless parameter, is defined as:

$$V = \frac{2\pi}{\lambda} a\sqrt{n_1^2 - n_2^2} = \sqrt{U^2 + W^2} \tag{3.8}$$

Numerically solving these equations, it is possible to obtain the propagation constants for arbitrary circular wires. Figure 3.2, for example, illustrates the effective refractive index ($n_{eff} = \beta/k_0$) dependence on the wire diameter for an air-clad silica wire at 800nm wavelength[2]. When the V-number is smaller than 2.405, only the fundamental mode HE_{11} is guided (solid line). When $V > 2.405$, several higher order modes coexist (dashed lines).

As the diameter is related to the V-number and the wavelength by $V = \frac{\pi}{\lambda} d\sqrt{n_1^2 - n_2^2}$, the single-mode condition, $V = 2.405$, states that the cutoff diameter is wavelength dependent. Figure 3.3 displays the single mode condition for air-clad and water-clad silica and tellurite micowires, the shaded areas below the curves corresponding to the single-mode regions. The smaller the light wavelength, the smaller the cutoff diameters; and

[2]The simulation considered the refractive index n_1 dependence on the wavelength given by the Sellmeyer equation [100].

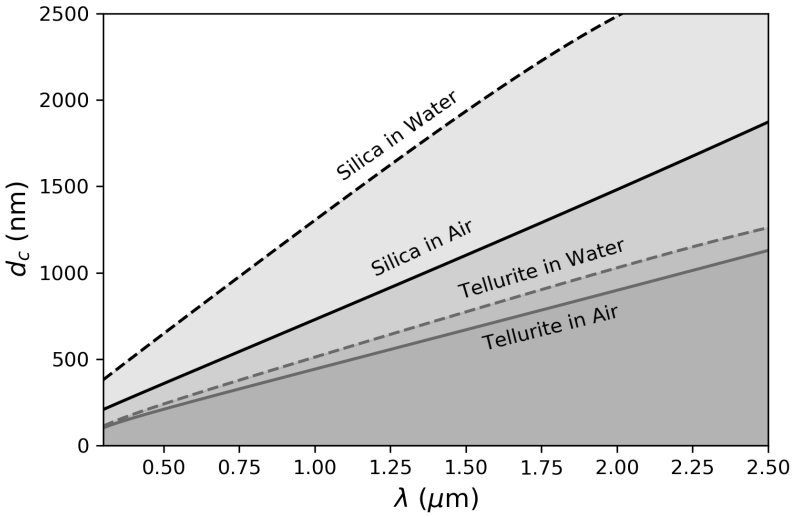

FIGURE 3.3: Single-mode condition for air- and water-clad, silica and tellurite wires

the higher the surrounding refractive index, the larger the cutoff diameters. In fact, ignoring the dispersion this is a linear relation ($d \propto \lambda$) with the proportionality constant $V/(\pi\sqrt{n_1^2 - n_2^2})$.

3.1.1 Power Distribution

The power distributions of the fundamental mode can be obtained as in reference [99] (section 12-7 to 12-10, pages 248–257). It is considered that there only exists energy flow in the z-direction. Thus, the power is represented by the Poynting vectors along zz, S_z. Figure 3.4 shows the power distribution of the fundamental mode for air-clad silica wires with 400 nm and 1000 nm diameters at 1550 nm wavelength. The confinement is diameter-dependent: while the 1000 nm wire confines most of the propagating power inside its physical boundary, on the 400 nm wire there is a large amount of power being guided as evanescent wave.

From the power distributions, it is possible to compute the fraction of power in the evanescent field (η_{EF}) from the Poynting components S_z by:

$$\eta_{EF} = \frac{\int_a^\infty S_z dA}{\int_0^a S_z dA + \int_a^\infty S_z dA} \tag{3.9}$$

where $\int_0^a S_z dA$ and $\int_a^\infty S_z dA$ correspond to the power inside and outside the wire, respectively, and $dA = r \cdot dr \cdot d\phi$ is the unit area. This quantity depends mainly on the

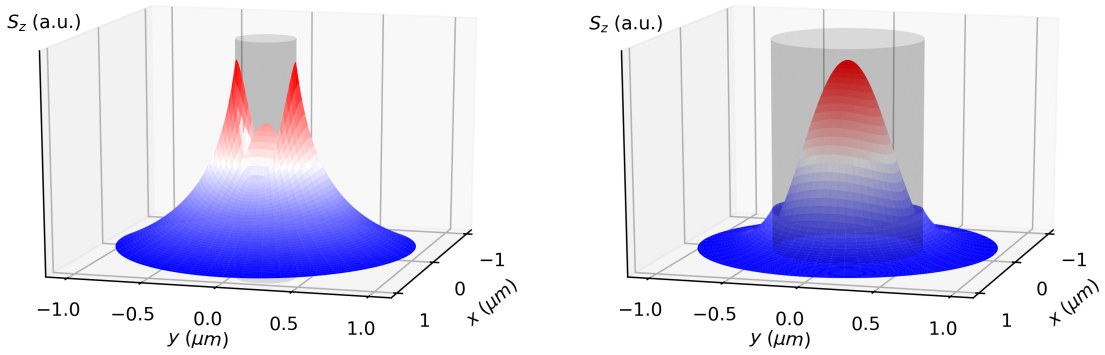

(A) $d = 400nm$ (B) $d = 1000nm$

FIGURE 3.4: Power distribution of the fundamental mode for 400 nm and 1 μm cylindrical wires at $\lambda = 1500$ nm wavelength.

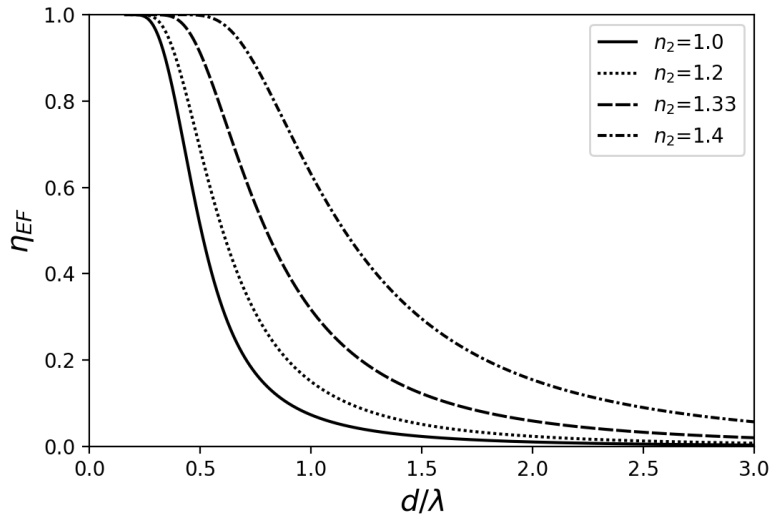

FIGURE 3.5: Fraction of Power of the fundamental mode propagating on the evanescent field (η_{EF}) of a silica wire as a function of the normalized wavelength, d/λ, for various surrounding refractive indices n_2 (Computations performed at 633 nm wavelength).

wavelength λ of guided light, the wire diameter d, and the index contrast with the surrounding environment. Figure 3.5 shows the dependence of η_{EF} on the normalized diameter (d/λ) for silica wires in different environments. Lower index contrast results in a higher amount of power in the evanescent field. As an example, for an air-clad silica wire, when the diameter is about half the wavelength, approximately 50% of power resides in the evanescent field.

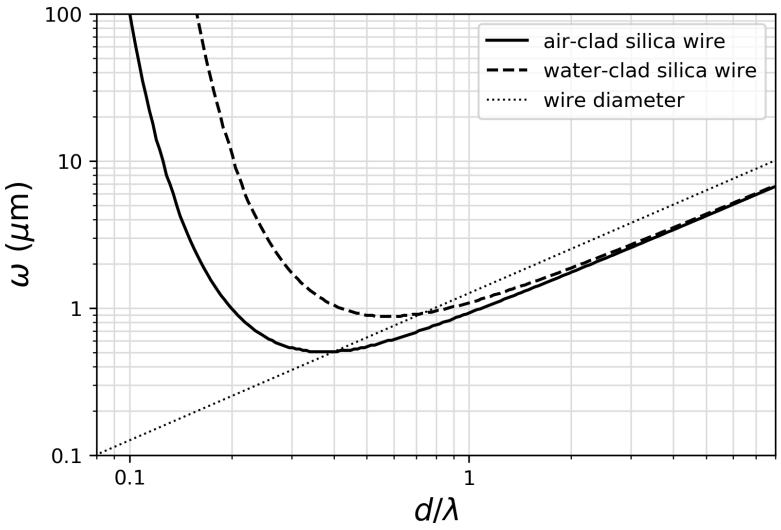

FIGURE 3.6: Effective diameter of the light profile of the fundamental mode for air- and water-clad silica wires. (Computations performed at 633nm wavelength)

3.1.2 Confinement

Another interesting quantity is the beam spot size ω, defined as the radial distance from the wire center at which the normalized intensity has dropped to $1/e^2 (\approx 0.135)$. The beam spot size decreases with the wire diameter, reaching a minimum given by the diffraction limit when d is of the order of 0.5λ (or $V \approx 2$), as shown in Figure 3.6. For even smaller diameters, the mode becomes less bound, extending way beyond the microwire's physical boundary.

3.2 Nonlinearity

In the high confinement region ($V \sim 2$), the beam spot size is at its minimum and the intensity is maximized. This maximizes the so called nonlinear quality factor γ

$$\gamma = \frac{2\pi}{\lambda} \frac{\bar{n}_2}{A_{\text{eff}}} \tag{3.10}$$

where $\bar{n}_2$ is the material nonlinear refractive index and $A_{\text{eff}} = \pi\omega^2/4$ the beam effective area.

Compared to standard telecom single-mode fibers, which have $\gamma \sim 10^{-3}$ $\text{W}^{-1}\text{m}^{-1}$, silica microwires have γ seventy times larger, and microwires from highly nonlinear materials, like As_2Se_3 glass, have γ 62000 times greater [101].

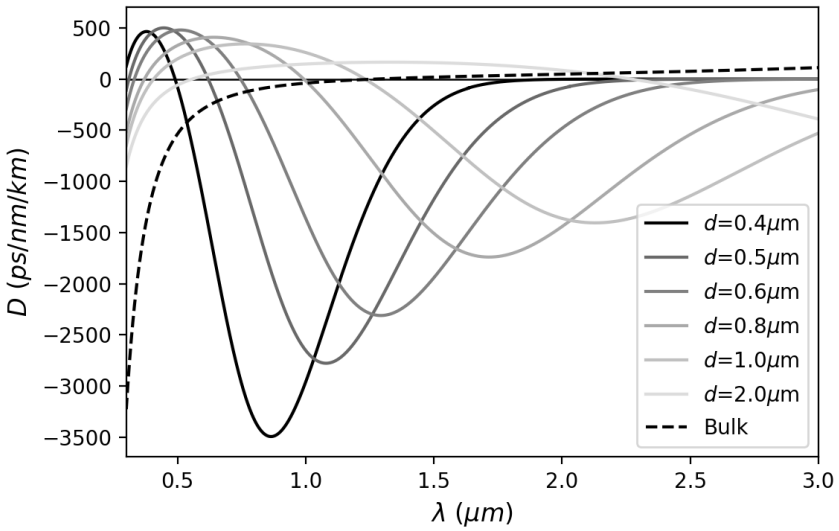

FIGURE 3.7: Waveguide Dispersion for air-clad silica wires with different diameters.

3.3 Dispersion

In Guided Optics, the Group Velocity Dispersion comes from the material and the waveguide geometry. In the submicrometric regime, the waveguide dispersion D_w becomes dominant, given by [99]:

$$D_w = \frac{d\left(v_g^{-1}\right)}{d\lambda} = \frac{d}{d\lambda}\left(\frac{c}{n_1^2}\cdot\frac{\beta}{k_0}\cdot\frac{1}{1-2\eta_{EF}\Delta}\right)^{-1} \tag{3.11}$$

The only yet undefined parameters are the group velocity v_g, the light speed in vacuum c, and $\Delta = \frac{1}{2}\frac{n_1^2-n_2^2}{n_1^2}$ the profile height parameter.

Figure 3.7 shows the dispersion spectra for microwires with several diameters. The diameter influences the dispersion greatly. As the diameter decreases, the zero-dispersion wavelength shifts to lower wavelengths, and a second zero-dispersion wavelength appears in the visible/near-infrared ranges, so that two regions of normal dispersion are separated by an anomalous dispersion region. The extreme thinning of the wire may give way to spectra with normal dispersion over the whole range.

This level of dispersion control is of great use for nonlinear applications.

3.4 Summary

Optical microwires exhibit extraordinary optical properties due to having diameters of the order of the wavelength of guiding light. The analytical expressions for light propagation in microwires are already well established from the electromagnetic theory, and simple results can be found with numerical methods.

Modal propagation depends strongly on the diameter of the wire. In fact, decreasing the diameter leads to the dissipation/cutoff of high-order modes. This will be verified experimentally in Chapter 7.

Depending on the diameter of the wire, the power distribution of the fundamental mode can give rise to extremely high or low optical confinement. The former is fundamental to nonlinear applications while the latter is ideal for optical sensing.

Chapter 4

Tapering Optical Fibers

The characteristics of light propagation in optical microwires were presented in the previous chapter. To gain a yet better grasp of the subject at hand, it is necessary to analyze the microfiber as a whole, considering the transition regions as well. These regions are responsible for the guidance of light from the untapered fiber to the microwire and, therefore, have great influence on the overall response of the optical microfiber. This chapter will provide some basic concepts on the shape and modal evolution along tapered fibers.

4.1 The Tapering Profile

In 1992, T. A. Birks and Y. W. Li published the article *"The Shape of Fiber Tapers"* in which a model for the geometric profile of a microfiber was presented [8]. This simple model established that the diameter profile of a taper can be predicted based on its fabrication parameters, namely the pulling velocities and the length of the *hot-zone* (the heated region of the fiber).

The model considers that the *hot-zone* is uniform and of such temperature that the fiber is only soft enough to be stretched and not otherwise deformed or evaporated. Figure 4.1 shows two diagrams at consecutive times, t and $t + \delta t$, of the tapering process. At time t a cylinder of radius r_w is being uniformly heated by the *hot-zone* of length L, and pulled apart symmetrically with velocities v. At time $t + \delta t$ the glass stretches to form a thinner cylinder of radius $r_w + \delta r_w$ and length $L + \delta x$. The length of the *hot-zone* is changed to $L + \delta L$ [3].

By Conservation of Volume:

[3] Some notes: δx is the change of the cylinder length and δl is the *hot-zone* change, and $\delta r_w < 0$ and $\delta t, \delta x > 0$

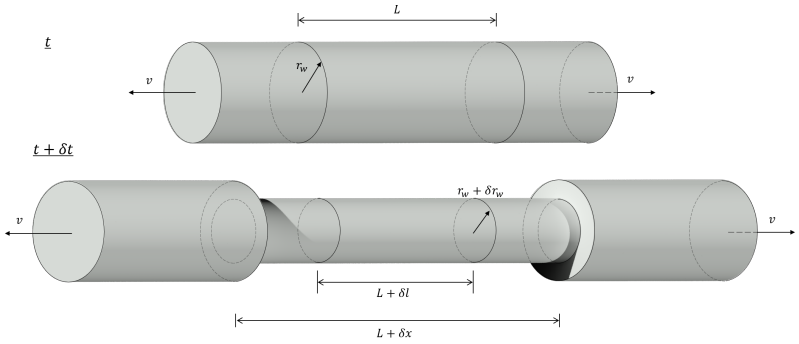

FIGURE 4.1: Diagram of the infinitesimal tapering process.

$$\pi {r_w}^2 L = \pi \left(r_w + \delta r_w\right)^2 \left(L + \delta x\right) \tag{4.1}$$

Rearranging the equation:

$$\left(\frac{r_w}{r_w + \delta r_w}\right)^2 = \frac{(L + \delta x)}{L} \tag{4.2}$$

For small variations ($\delta r_w \ll r_w$), the left term can be approximated to:

$$\left(\frac{r_w}{r_w + \delta r_w}\right)^2 = \left(\frac{1}{1 + \delta r_w / r_w}\right)^2 \approx 1 - 2\frac{\delta r_w}{r_w} \tag{4.3}$$

In the limit $\delta t \to 0$, the last equations can be grouped into:

$$\frac{dr_w}{dx} = -\frac{r_w}{2L} \tag{4.4}$$

Considering that the *hot-zone* length may vary in time it is possible write $L = L(t)$. And since x is an increasing function of time—the fiber is being pulled apart over time—L is a function of x: $L = L(x)$

Integrating both variables

$$\int_{r_0}^{r} \frac{dr_w{}'}{r_w{}'} = -\frac{1}{2}\int_0^x \frac{dx'}{L(x')} \tag{4.5}$$

with r_0 being initial fiber radius. A general expression relating the radius of the fiber waist, r_w with the total pulling length, x is, then:

$$r_w(x) = r_o \exp\left[-\frac{1}{2}\int_0^x \frac{dx'}{L\left(x'\right)}\right] \tag{4.6}$$

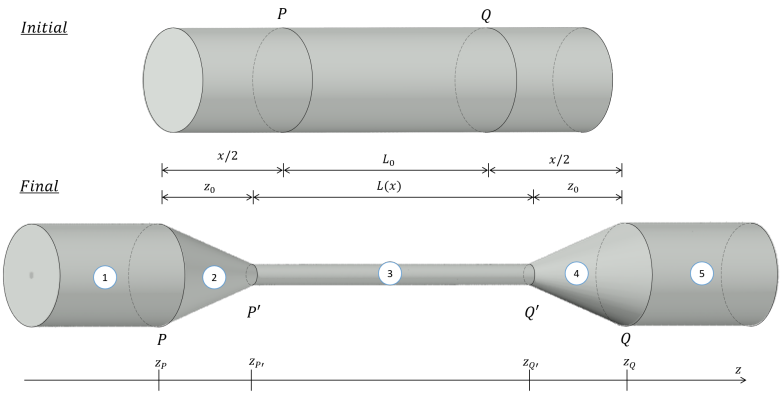

FIGURE 4.2: Comparison between the initial fiber (top) and the resulting taper (bottom).

It is also convenient to have an expression for the radius evolution along the fiber axis (the *taper profile*). Relating z to r and L (Figure 4.2):

$$L(x) + 2z_0 = x + L_0 \tag{4.7}$$

Any further development of this model needs an expression for $L(x)$, which can be arbitrary as long as $L \geq 0$.

4.1.1 Constant *Hot-zone*

The simplest case is that of a constant *hot-zone*. Considering $L(x) = L_0$, then $z_0 = x/2$ is the pulling length of a single pulling stage. The analytical solution to equation 4.6 becomes:

$$r_w(x) = r_0 e^{-x/2L_0} \tag{4.8}$$

and the taper profile can be defined by:

$$r(z) = \begin{cases} r_0 & \text{for } z < z_P \quad \text{(region 1)} \\ r_0\, \mathrm{e}^{-(z-z_P)/L_0} & \text{for } z_P < z < z_{P'} \quad \text{(region 2)} \\ r_0\, \mathrm{e}^{-x/(2L_0)} & \text{for } z_{P'} < z < z_{Q'} \quad \text{(region 3)} \\ r_0\, \mathrm{e}^{(z-z_Q)/L_0} & \text{for } z_{Q'} < z < z_Q \quad \text{(region 4)} \\ r_0 & \text{for } z > z_Q \quad \text{(region 5)} \end{cases} \tag{4.9}$$

In this model, the shape of a fiber taper is completely defined by the *hot-zone* and the pulling length. For example, Figure 4.3 shows the theoretical results for (A) the waist

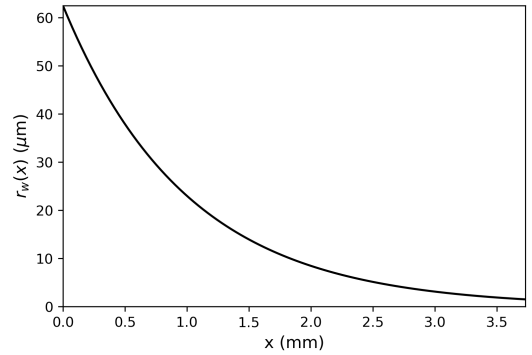

(A) waist radii *vs* pulling length

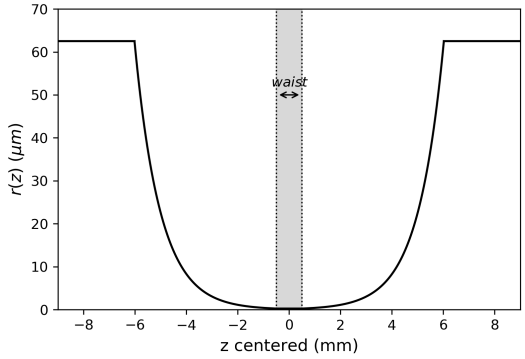

(B) Taper Profile

FIGURE 4.3: Plotting of the Birks' model for fiber tapering, considering $r_0 = 62,5\mu$m and $L_0 = 1mm$.

radius dependence on the pulling length and (B) the taper radii profile for the tapering of a 125 μm fiber with a constant *hot-zone* of $L_0 = 1$ mm.

4.2 Modal Evolution on a Tapered Fiber

In the previous section, a simple model for the shape of fiber tapers was analyzed. However, light propagation in optical microfibers was overlooked. Considering that the transition regions are smooth enough so that no power coupling occurs between modes (see Appendix C), the modal evolution in a tapered fiber is straightforward. Figure 4.4 shows both a schematic and the numerical simulations for the beam spot size of the modal evolution in a taper, indicating several confinement regions.

In a standard telecom single-mode optical fiber, the light is guided on the core-cladding interface (A). Decreasing the fiber diameter will lead to the light being focused on the core

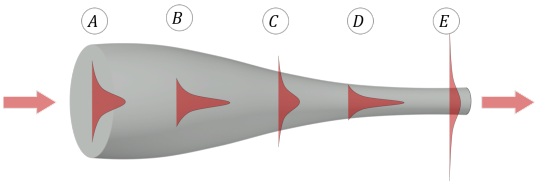

(A) Diagram

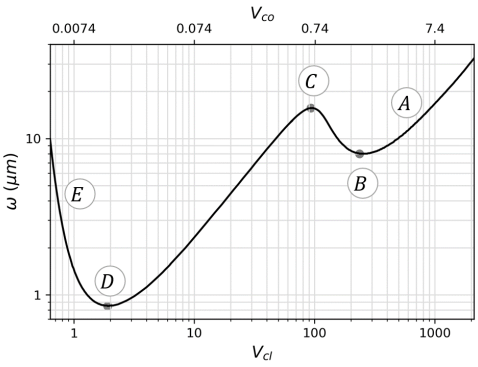

(B) Beam spot size *vs* cladding (bottom) and core (top) V numbers

FIGURE 4.4: Modal evolution in a tapered fiber.

until maximum confinement occurs (B). The mode then expands, becoming guided in the cladding-air interface (C). Further decreasing the diameter leads to focusing of the light in the cladding, and the beam spot size reaches its absolute minimum value (D). For even smaller diameters, the radiation becomes less and less bound, propagating mostly as evanescent wave (E).

4.3 Summary

This Chapter ends the theoretical exposition of the optical microfibers' properties. The shape of the microfiber is directly related to the fabrication parameters. A simple model for the symmetrical pulling of a fiber considering a constant *hot-zone* has well defined analytical solutions, and the validity of this model will be experimentally analyzed in Chapter 6.

A diagram of the modal evolution along the length of a tapered fiber is presented. Several distinct confinement regions occur, enabling a wide range of applications.

Chapter 5

Taper Fabrication using an Electric Microheater

This thesis will explore the production and characterization of optical microfibers fabricated by electric microheating. However, at the beginning of this work the tapering rig was unassembled. Therefore, most of the working time was devoted to the implementation and optimization of the tapering apparatus.

This Chapter will provide a thorough report on the experimental setup and the tapering process. All main components of the apparatus will be exposed and commented, and the tapering sequence—the steps to the successful fabrication of the microfibers— will be detailed.

5.1 Experimental Setup

The assembling and optimization of the tapering apparatus evolved through several versions until a somewhat final setup was chosen. However, with the unfolding of the work, it was found that some elements of this apparatus still needed some improvements. To prevent constant minor changes that could affect the overall analysis of results, the final version was left unaltered, with its pros and cons examined as they become apparent. Several possible improvements are discussed in Chapter 9.

This setup relies on a heat-and-pull technique using an electric microheater as a heat source and two motorized linear stages as pulling elements. The tapering setup is schematized in Figure 5.1 and pictured in Figure 5.2.

In the following sections the setup's main components will be presented.

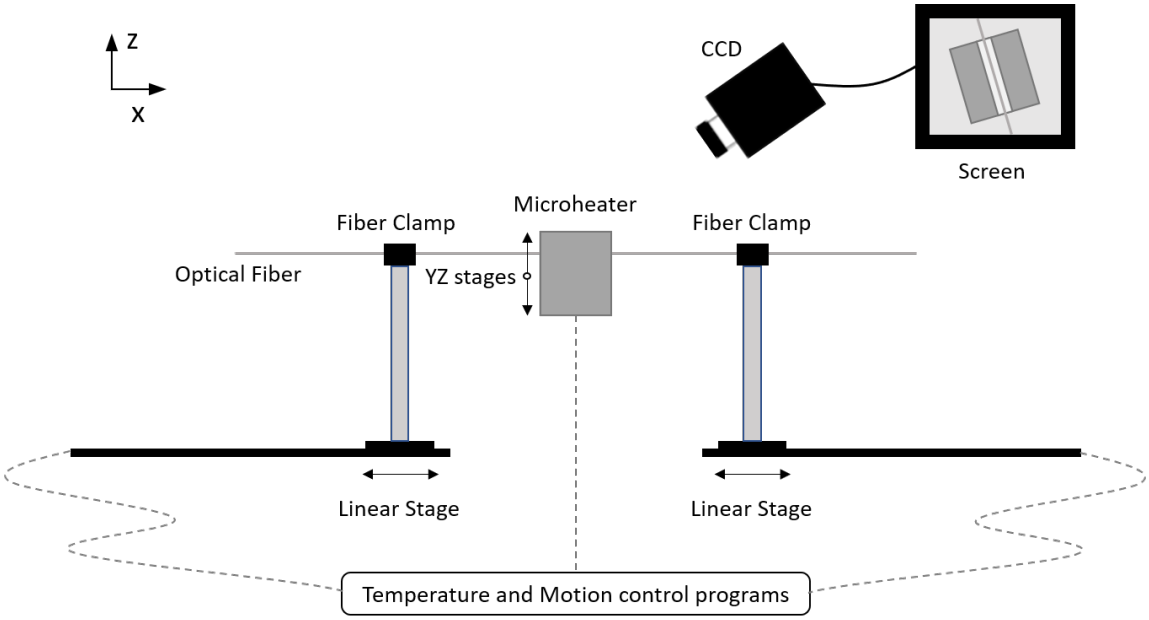

FIGURE 5.1: Schematic of the tapering rig.

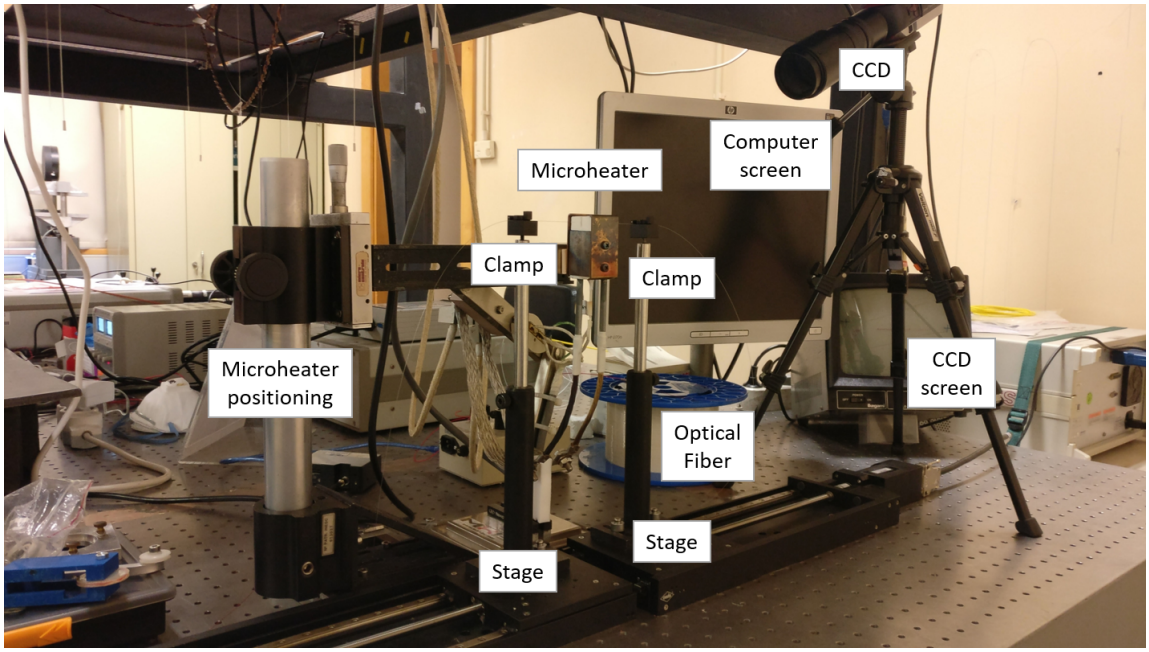

FIGURE 5.2: Photograph of the tapering rig.

5.1.1 The Microheater

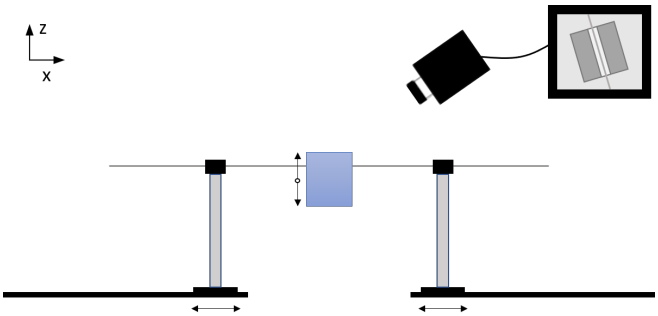

FIGURE 5.3: Schematic of the tapering rig, with the microheater highlighted.

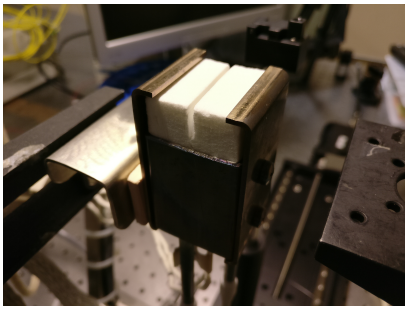

FIGURE 5.4: Photograph of the microheater.

The main component of this rig is the heating source (highlighted in Figure 5.3). In this project it was used the MHI MicroFiber^{TM} Heater *FibHeat 200* electric microheater (Figure 5.4). This is a compact (33×30×58 mm case and 2×30×10 mm slot), high temperature (1900°C maximum element temperature) heating element that can heat an optical fiber into a softened state, allowing for efficient pulling. Further information on the microheater's specifications can be accessed in Table A.1, Appendix A.

The heater unit comes provided with a Type "B" thermocouple located inside the ceramic and close to the heating element. However it will be reading neither the actual temperature of the heating element nor the temperature on the fiber slot. To lessen reading errors, MHI supplies a calibration chart relating the temperatures presented by the thermocouple readings with the 'actual' temperatures (read using a infrared pyrometer), which can be seen in Figure A.1, Appendix A. As the actual value of the temperature does not factor in the tapering technique, this calibration chart was followed roughly without any apparent disadvantage.

As for communication, the microheater can be controlled using an Eurotherm 2416 Temperature Controller, allowing for the implementation of specific temperature sequences. This can also be done remotely using the software provided by the manufacturer.

5.1.2 The Traveling stages

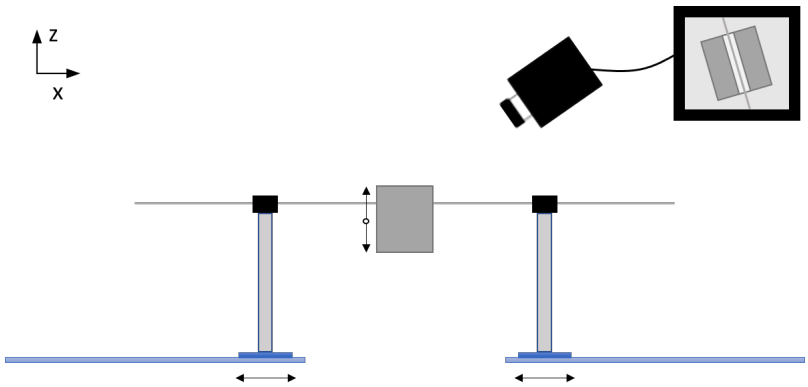

FIGURE 5.5: Schematics of the experimental setup, with the pulling stages highlighted.

The positioning and pulling of the fiber was achieved by two precision linear translation stages *LTM 120* from OWIS® (highlighted in Figure 5.5). These stages can produce linear velocities up to $10mm/s$ and guarantee position errors of less than $25\mu m/100mm$. In practice, the range of velocities implemented was $10-100\mu m/s$ and thus easily obtainable by the stages; the positioning resolution of $25\mu m$ was observed experimentally.

The stages were computer operated by two *Position Control Units PS 10* in addition to the proprietary software OWISoft. In certain configurations, it is possible to operate multiple stages using a single controller. This situation is different, as two separate control units were used which resulted in a slight lag between the two stages. Considering the low, constant speeds used, this ended up being an insignificant issue. The movement of the stages was easily customized with OWISoft's intuitive programming utilities.

5.1.3 The Optical Fiber

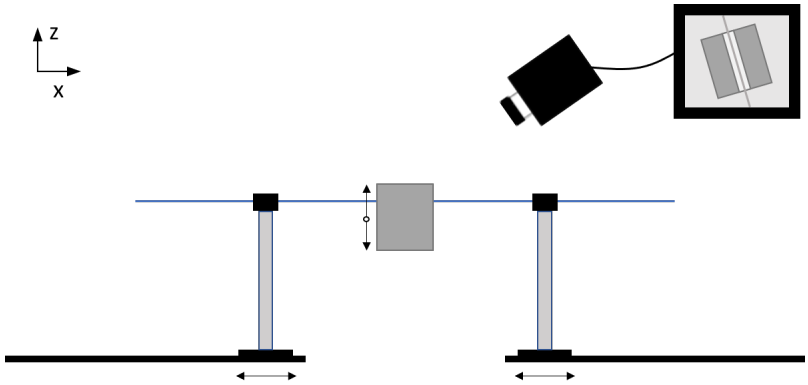

FIGURE 5.6: Schematics of the experimental setup, with the fiber highlighted.

To ensure uniformity in the results, all microfiber tapers were fabricated from the same optical fiber spool: a *Corning® SMF-28e+®*. This is a 125 μm-cladding step-index optical fiber, single-mode at $\lambda > 1260\ nm$, widely used in optical communications. A detailed specification sheet can be seen in Table 5.1, and the location of the optical fiber in the fabrication setup is highlighted in Figure 5.6.

Index Profile	Step Index
Core Diameter	8.2 μm
Cladding Diameter	125 ± 0.7 μm
Coating Diameter	242 ± 5 μm
Numerical Aperture	0.14
Maximum Attenuation	$\leq$ 0.20 dB/km @1550 nm
Mode-Field Diameter	10.4 ± 0.5 μm @1550 nm
Dispersion	$\leq$ 18.0 ps/nm/km @1550 nm

TABLE 5.1: Technical specifications of the Optical Fiber [102].

5.1.4 Fiber clamps and General Alignment

The alignment of the fiber with respect to the microheater slot is of capital importance. The main components responsible for alignment are highlighted in Figure 5.7. Some aspects need to be considered. First, the fiber support: both ends of the optical fiber are fixed using magnetic clamps. Due to the height of the microheater related to the optical table, it was necessary to elevate the fiber clamps, which was accomplished with metallic posts. However, their cylindrical geometry brought some rotational inaccuracy to the setup. In fact, as seen in Figure 5.8, even a slight misalignment between the clamps can lead to catastrophic results, as the fiber bends inside the microheater and can, in the worst-case

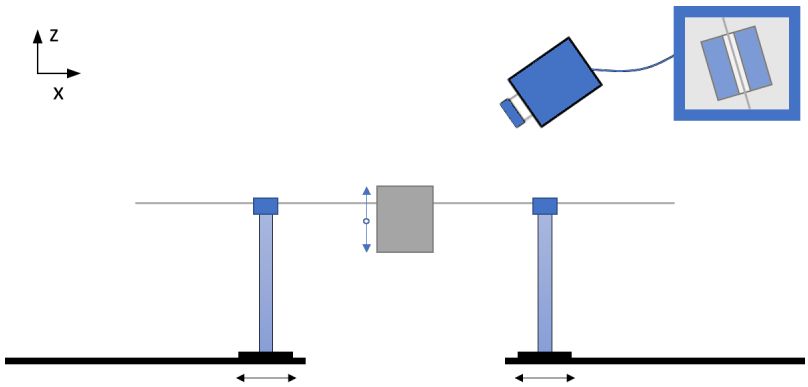

FIGURE 5.7: Schematics of the experimental setup, with the alignment elements highlighted.

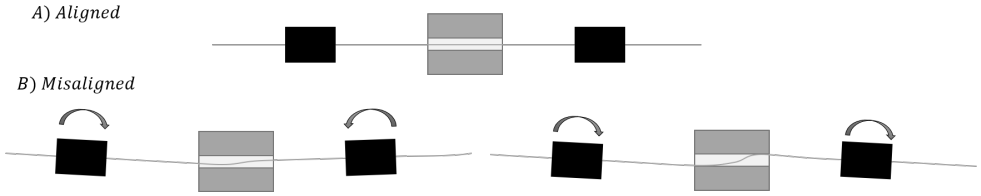

FIGURE 5.8: Misalignment between the fiber clamps and its effect on the taper path.

scenario, hit its walls. It was found that this happens mainly for thinner tapers ($\leq 3\mu$m waist diameters), since the clamps are farther apart and the fiber is more flexible. To ensure result homogeneity and have some presentable work in the allotted time, this was something that was only mitigated and left pending as of the writing of this dissertation. Some possible improvements are presented in Chapter 9.

The alignment aspect of the setup is finished by the implementation of two manual linear stages on the microheater, on the Y and Z axis. These handle the alignment of the fiber and the heating slot, and isolate the microheater from the rest of the setup once the tapering process is completed. To avoid eye exposure to the blinding light emitted by the microheater when at high temperature, the manual alignment is aided by real-time monitoring using a CCD.

5.2 Tapering Sequence

The fabrication of the microfibers is relatively simple, consisting in heating and pulling an optical fiber. In practice, however, it is somewhat problematic, and there are some particularities to consider. Thus, this section will list and examine the various steps necessary for microfiber fabrication, from pre- to post-processing.

5.2.1 Microheater Temperature

The first thing to do, even before preparing the fiber to use, is to turn on the microheater and heat it to the desired temperature. As reported earlier, this step can be automated using the microcontroller and the provided software. Figure 5.9 shows the usual heating profile[4].

The temperature is increased 'manually' at 50 % current (approximately 30A) until the termocouple reads 300°C (dotted line). This manual step is necessary since the termocouple is inaccurate for low temperatures and, if in automatic mode, the controller sets the microheater to full power (100% current intensity) which may damage it in the long run.

After reaching the 300°C mark, it is best to change the operation to automatic and run the desired profile program. In this case, the microheater is heated to 900°C at a rate of 15°C/min and then to 1010°C at 10°C/min. After reaching 1010°C, the optimal

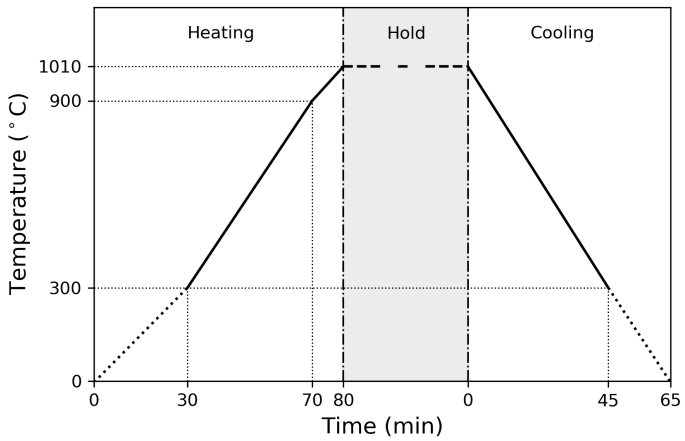

FIGURE 5.9: Temporal evolution of the temperature for the tapering process.

[4]The temperature values presented in Figure 5.9 do not reflect the actual temperature on the fiber slot. A calibration chart is presented in Appendix A.

temperature for tapering, obtained by trial and error, the program is put on hold (dashed line in Figure 5.9), and it is possible to start the fiber tapering.

5.2.2 Fiber Preparation

Before pulling, roughly 120 mm of the fiber's protective coating is removed with a regular fiber optic stripper. The uncoated fiber is then thoroughly cleaned with ethanol and fixed, tensioned, on the fiber clamps. To keep track of possible slipping of the fiber on the clamps, two dots are made next to the fiber clamps, with a permanent marker.

5.2.3 Fiber Pulling

With the fiber already cleaned and fixed in place, the microheater at the desired temperature, and the pulling stages initialized, it is possible to fabricate the desired microfibers.

First, the microheater is brought to place. To ensure uniform results, the elevation of the fiber on the slot is always the same on different tapering attempts. This is accomplished with the aid of a marker on the Z-axis stage of the microheater, set by trial and error, as the fiber should be close enough to the heating element so that the local temperature is hot enough to soften it, but high enough on the slot so that post-pulling extraction is uncompromised.

After setting all the elements into place, the fiber is left to rest around one minute inside the microheater, so that it can reach thermal equilibrium. Starting the pulling any sooner usually lead to the slipping of the fiber on the clamps, as the fiber did not reach the softened state.

The fiber pulling was then started. Since this was a first foray into this setup, it made sense to begin with the simplest pulling case: traveling stages at constant velocity. Thus, the stages were set to move at the same speed in opposite directions.

When the taper reached the desired length, the program was manually halted. The microheater was then immediately isolated from the rest of the setup to allow for the withdrawal of the fabricated fiber taper.

5.2.4 Taper Holder

One of the main obstacles encountered during the development of this work was the withdrawal of the fabricated taper from the setup. This was because the taper, especially for smaller waist diameters (20μm or less), was extremely fragile to strain. When time

came to remove the fiber from the magnetic clamps, it often became stuck on the top rubber of the clamp and exerted such a transverse force that resulted in the breakage of the microfiber at the waist. Figure 5.10 shows a simplified scheme of this behavior. Notice that, even when both clamps were opened at the same time (not pictured) the result was the same: the taper broke.

FIGURE 5.10: Unsuccessful withdrawal of the microfiber.

To solve this problem, something was needed to hold the taper in place so that the clamps could be opened without the above mentioned fault. Moreover, since the main goal was to remove the fiber from the rig, it would be good to have this solution also serve as a means to transport the microfiber to another location, being it to be stored for later use or to any other kind of setup, to be characterized.

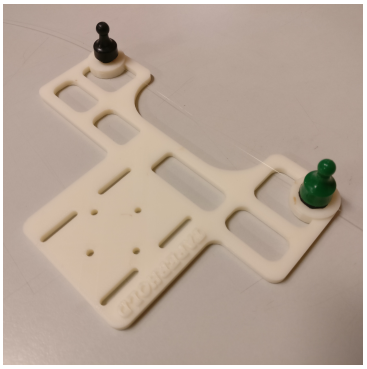

FIGURE 5.11: The Taper Holder carrying a microfiber (Refer to Appendix B for the specifications sheet)

Thus, a Taper Holder, which can be seen in Figure 5.11, was designed and 3D printed. This structure is sturdy, lightweight, and versatile, since it can be placed in different setups thanks to its hole arrangements.

In order for it to be able to relocate the fiber, it had to hold it temporarily. This was accomplished magnetically, by gluing two neodymium magnets at the bottom of the Taper Holder and using two other padded magnets to secure the fiber.

Figure 5.12 shows the proceeding to successfully withdraw the fabricated taper from the pulling apparatus. The Taper holder is fixed in a support that is slowly elevated until it touches the fiber taper—the points of contact are close to the clamps and so the taper in itself is undisturbed—. Sponge padded magnets are then used to fix the taper, and the clamps are safely opened without breaking it. The Taper Holder is then used to relocate the microfiber.

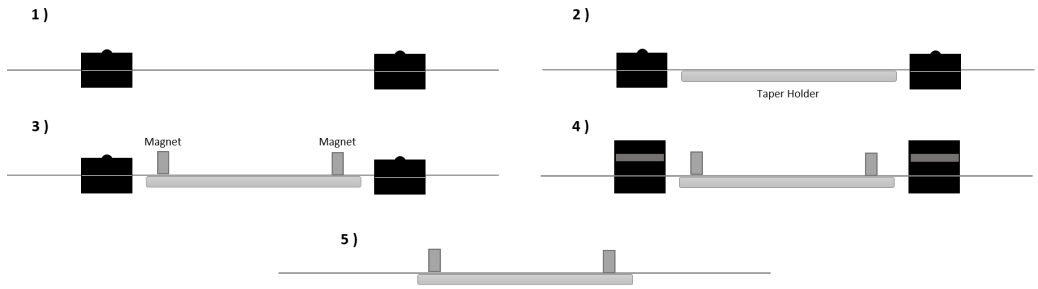

FIGURE 5.12: Steps for the successful withdrawal of the fiber from the rig.

5.2.5 Storage

The fabricated microfibers were stored vertically, being taped at one end to ledges placed on the laboratory walls. Being fastened on one end made sure that there was no undesired tension on the taper, and the ledge was such that the taper region was far from touching the walls and degrading in the process.

5.3 Summary

This Chapter detailed all things related to the fabrication of optical microfibers, from the setup's main physical components to the tapering process' steps.

The tapering rig relies on the *Modified Flame Brushing Technique* using an electric microheater and two motorized pulling stages. These two main components can be controlled externally using software provided by the manufacturers.

It was found that the alignment of the whole apparatus is the limiting factor for the fabrication of the microfibers, in such a way that microfibers with waist diameters lower than 3μm were hard to fabricate and reproduce.

Due to the frailty of the microfibers, a structure was developed in order to aid the removal of the fiber from the rig and consecutive relocation.

Chapter 6

Microfiber Shape

The previous Chapter provided a detailed analysis of the microfiber fabrication process using an electric microheater. The characterization of the resulting structures, which may allow for the optimization of the fabrication process and tailoring of the microfibers for applications, is the natural next step.

An untapered optical fiber is already hard to discern with the naked eye, being 125 μm thick, and transparent. So, it is easy to understand that the task of characterizing microfibers is delicate and complex. In this Chapter the methods and results of the profiling of optical microfibers will be discussed, and compared to the model presented in Chapter 4.

6.1 The Fabricated Microfibers: An Overview

Tapers with waist diameters as low as 1.5 μm were fabricated during this work. Due to their optical properties, microfibers with waists smaller than 20 μm were particularly interesting. Unfortunately, small misalignments on the tapering process made microfibers with waists thinner than 5 μm hard to reproduce, since most of the time they hit the walls of the microheater and broke. Regardless, a sufficient number of microfibers were fabricated in order to take some conclusions.

Macroscopically, the fabricated microfibers, and especially when thinner than 20 μm, are extremely hard to discern with the naked eye, their visibility depending greatly on the lighting conditions. From end to end, the microfibers are long and present smooth transition regions. Mechanically, they are quite flexible, being relatively easy to bend and even make loops. However, the manipulation of the microfibers is a delicate subject.

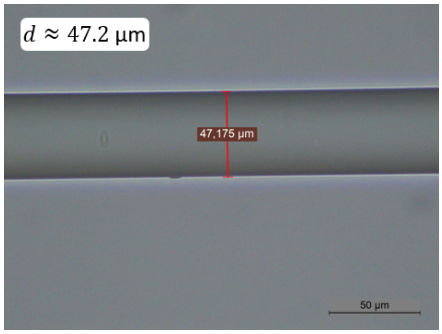

(A) $d \approx 47,2\mu$m

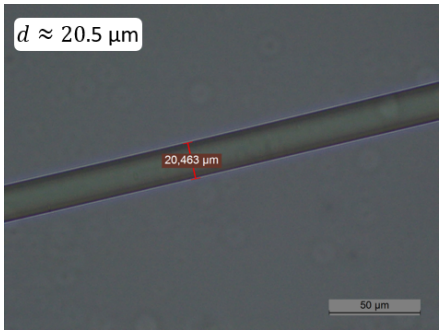

(B) $d \approx 20,5\mu$m

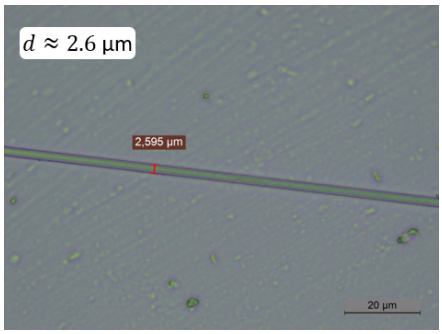

(C) $d \approx 2,6\mu$m

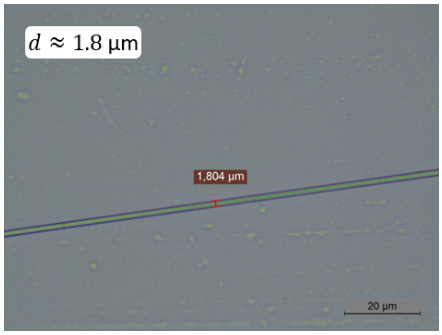

(D) $d \approx 1,8\mu$m

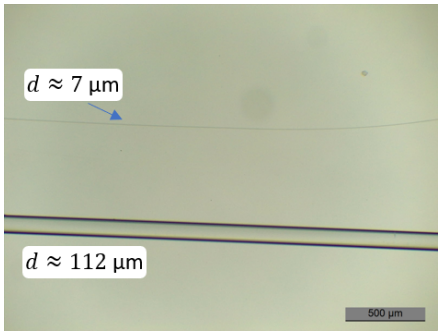

(E) A $d \approx 112\mu$m and a $d \approx 7\mu$m taper side by side

FIGURE 6.1: Optical Microscope images of some microfibers

It was found that holding the microfibers at one end was, apart from the taper holder discussed in Chapter 5, the best way to ensure their preservation.

The first analysis of the microfibers was performed with the *Leica DM500* optical microscope and related image capturing and processing elements *(Leica ICC50W* & *Leica LAS*). The microfibers were taped to glass slides ($26 \times 76 \times 1$ mm) before being processed under the microscope. Figure 6.1 shows several images of the waists of some microfibers. This tapering method can result in very thin microfibers. It was also verified that the transition regions are very smooth, the waist is uniform, and the taper has little surface roughness[5].

[5]further analysis of the roughness would have to be performed by Scanning Electron Microscopy (SEM).

6.2 Taper Geometry

The geometry of a microfiber is strongly connected to its optical properties and has significant implications on the kinds of applications it can be used in. In the following sections, a detailed analysis of the geometric features of the fabricated microfibers will be performed.

6.2.1 Waist Diameter

The profile of a microfiber can be predicted by the fabrication parameters. As seen in Chapter 4, Birks' model associates the microfiber shape with the length of the *hot-zone* and the pulling length of the stages [8]. So, it is logical to relate the taper's waist diameter with a pulling length.

In literature, it is common to refer to the total pulling length, the difference between the final and initial separations of the pulling stages. However, in this fabrication process, the control is handled individually and only the pulling length of the individual stages—the *single-stage travel*— is provided by the controlling software. As the stages move symmetrically, the single-stage travel is half the total pulling length.

Several microfibers were fabricated for single-stage travels in 2,5 mm increments, roughly. They were then taped to glass slides and processed under the microscope with the waist location determined visually. Figure 6.2 relates the waist diameter with the single-stage travel.

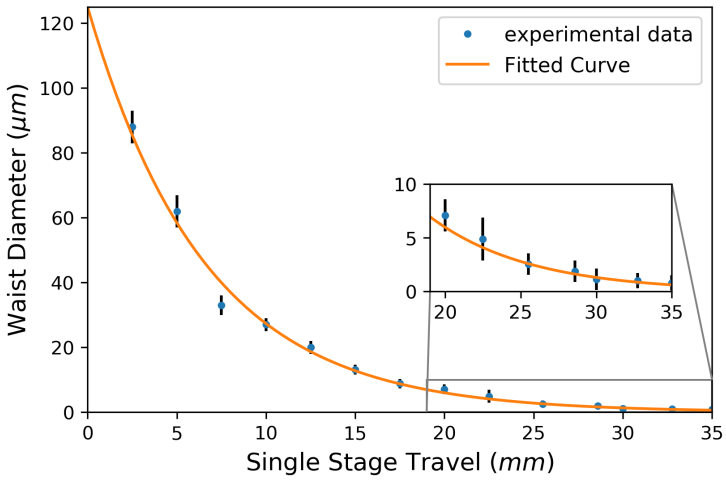

FIGURE 6.2: Waist diameter as a function of the single-stage travel.

The experimental data (markings) seems to exhibit a decreasing exponential behavior. Adapting equation 4.8, it was expected:

$$d_{waist}(x) = d_0 e^{-x/L_0} \tag{6.1}$$

where d_0 is the original fiber diameter, L_0 is the *hot-zone* length, and x is the single-stage travel.

Fitting the data to this expression, considering $d_0 = 125$ μm, it comes:

$$\begin{gathered} d_{waist}(x) = 125 e^{-x\ (mm)/(6.6\pm0.2)\ (mm)}\ (\mu m) \\ r^2 = 0.992 \end{gathered} \tag{6.2}$$

The waist diameter evolution follows the theoretical behavior given from Birks' model. To give a physical meaning to the fitting value, $L_0 = 6,6 \pm 0.2$ mm should correspond to the *hot-zone* length. Considering that the fiber slot on the microheater is 30 mm long, this value seems acceptable, although somewhat small.

This relationship became extremely useful for the rest of this work since it served as a guide for the fabrication of specific tapers. Some important diameter values and their corresponding single stage travels are shown in Table 6.1. This, however, is not foolproof as, when the fiber slips on the clamps, these projections can be inaccurate.

Diameter (μm)	Single Stage Travel (mm)
50	6.03
25	10.57
10	16.61
5	21.17
2.5	25.73
1	31.75

TABLE 6.1: Some diameter values and corresponding single stage travels.

6.2.2 Taper Profile

Another crucial geometric property to analyze is the taper profile, i.e. the diameter evolution along the taper length. Given that these are long microfibers (≈40 mm from end to end on a 5 μm microfiber, for example), it would be impractical to profile it using the optical microscope, as it would be necessary to keep continually refocusing and analyzing the image. Additionally, placing the microfibers on glass slides degrades them.

Some simple, contactless method was needed. A quick literature search provided some alternatives, adopting: CCD imaging [103], Whispering Gallery Modes [104], and

Light Diffraction [105]. Due to its simple nature and ease of implementation and analysis, a diffraction apparatus was assembled.

6.2.2.1 Diffraction Setup

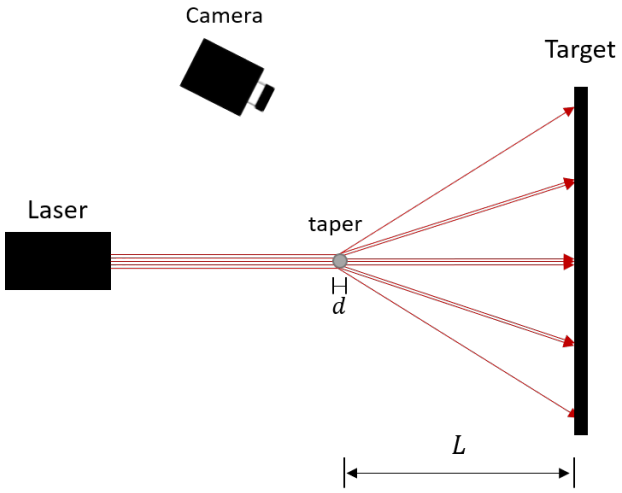

FIGURE 6.3: Diagram of the diffraction setup for diameter measuring. (Top View)

The assembled diffraction apparatus for taper profile measurements is relatively simple (Figure 6.3). Its underlying principle is that the beam of a HeNe laser ($\lambda = 633$ nm), when directed at the microfiber is scattered and forms an intensity pattern on the target (the wall of the laboratory).

6.2.2.2 Diffraction Pattern

The interference pattern consists in alternating bright and dark regions. Figure 6.4 shows an example of the diffraction pattern on the target, at a distance L from the fiber. The graded ruler above the pattern serves as scale bar for posterior analysis.

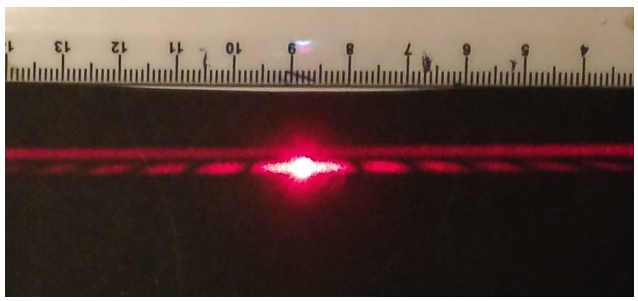

FIGURE 6.4: Photograph of a diffraction pattern.

Despite being a rather simple pattern, some observations are in order:

- The center's light intensity comes from the direct ray and could have been reduced if some absorbent element, like the hole in reference [105], had been added.
- The diffraction pattern spreads for thinner diameters and contracts for higher diameters. In consequence, for untapered fibers, the intensity peaks were too close together, and for thinner waists, they were so spread out that sometimes a satisfactory photograph of the pattern was challenging to obtain. In that case, a second target, closer to the microfiber, had to be placed. The ideal case would be that of a movable target.
- The line above the pattern is caused by the glass fiber acting as a cylindrical lens, and its location depends on the inclination of the microfiber. In some instances, this line interfered with the diffraction pattern, spoiling the results.
- The efficiency of the diffraction experiment could have been improved if the beam diameter had been decreased using a set of lenses.

6.2.2.3 Pattern Analysis

The intensity profile of the diffraction pattern was quantified using an image processing computer program (FiJi, a distribution of ImageJ). A linear path along the diffraction pattern was selected, and the program automatically calculated each pixel's intensity on a grayscale value. The resulting plot is shown in Figure 6.5.

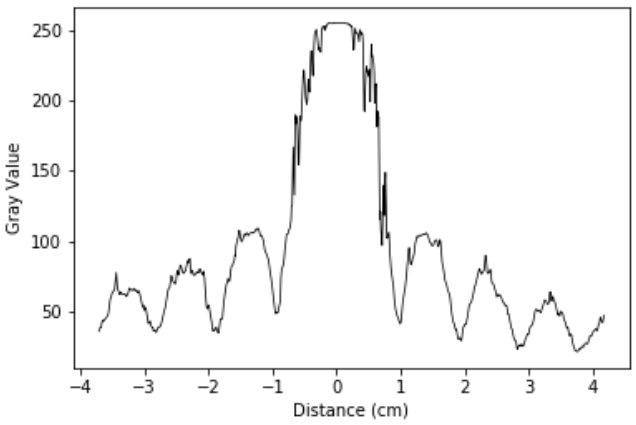

FIGURE 6.5: Intensity plot of the diffraction pattern.

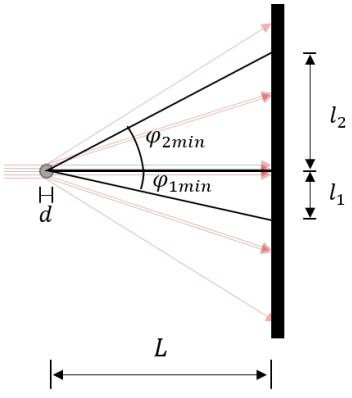

FIGURE 6.6: Geometrical analysis of the diffraction pattern.

The numerical analysis of the intensity plot was performed as in reference [105]. The diameter, d, of the illuminated spot of the microfiber can be given by:

$$d = \frac{4\lambda}{2\varphi_{1\,\mathrm{min}} + \varphi_{2\,\mathrm{min}}} \tag{6.3}$$

where λ is the wavelength of the laser beam, and $\varphi_{1\,\mathrm{min}}$ and $\varphi_{2\,\mathrm{min}}$ are the angles of the first and second minima of the diffraction pattern (refer to Figure 6.6 for a visual clue):

$$\varphi_{1,2\,\mathrm{min}} = \arctan\frac{l_{1,2}}{L} \tag{6.4}$$

The intensity profile was smoothed and the positions of its minima were calculated. The diameter is given by Equation 6.3. in the shown pattern, $d \approx 17.5\ \mu$m.

6.2.2.4 Taper Profile: Results

Repeating the previously mentioned analysis for diffraction patterns taken along the microfiber length, it is possible to measure its profile. Figure 6.7 shows an example. The dots represent the experimental data: the calculated diameter values; the solid curve is an interpolation of these values; and the dotted curve corresponds to the theoretical profile given by equation 4.9, considering $L_0 = 6.6$ mm and pulling halted at 9.93 mm single-stage travel.

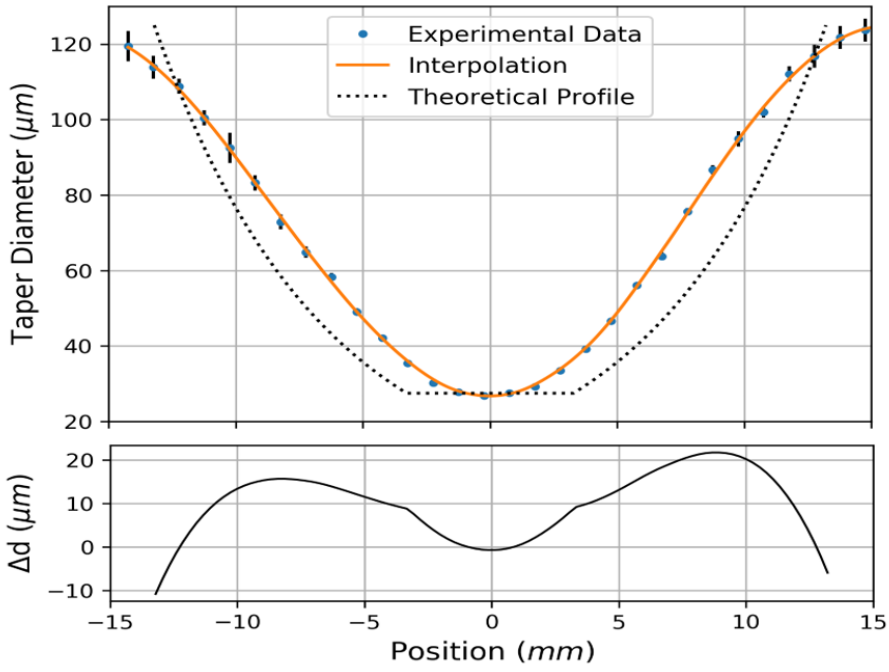

FIGURE 6.7: Example of a taper profile and its deviation from the theoretical profile.

.

The interpretation of Figure 6.7 can be divided in the following topics:

Taper Profile The tapered section is around 30 mm long with smooth transition regions and the microfiber is symmetric, as expected given that the stages travel at the same speed in opposite directions.

Waist Diameter The waist diameter calculated by diffraction is coherent with the theoretical value. According to the fitting equation 6.2, ending the tapering at 9.93 mm would result in a microfiber with a $d_{theor} = 27.6$ μm waist diameter. The minimum diameter calculated by diffraction was $d_{diff} = 26.8$ μm, meaning a 2.9% error. These values are also in agreement with the processed diameter with the optical microscope: $d_{micros} = 27.9$ μm.

Theoretical Profile The deviation of the experimental profile from the theoretical model is not surprising. The differences come from the fact that the model considers the idyllic case of a constant-temperature, abrupt-walled *hot-zone*, and neglects variables such as stage velocity and fiber viscosity. While it may give good results for a small *hot-zone*, for a longer heat source it needs some adjustments. A detailed model for the shape of fiber tapers, considering fluid mechanics can be found in reference [103].

Other Considerations There seems to be an inconsistency between section 6.2.1 and this one, concerning the validity of the theoretical model. Previously, the theoretical model was found to fit the obtained results for the relation between the waist diameter and the pulling length. However, Figure 6.7 shows the disparity between the microfibers and the model. Nonetheless, equation 6.2 still rules the waist diameter evolution. It is simply that the fitting parameter $L_0 = 6.6$ mm can no longer be attributed to the physical meaning of corresponding to the *hot-zone* length. Indeed, this could have been already predicted, as L_0 is smaller than the microheater length.

The measured diameter profiles of several other microfibers are shown in Figure 6.8. The dots represent the experimental data, and the solid lines are fits.

The same analysis applies. In fact, each thinner microfiber seems like the result of the continuation of the tapering process for the previous tapers. This means that the tapering setup is performing as expected. In the thinnest microfiber (in red, #4) there seems to

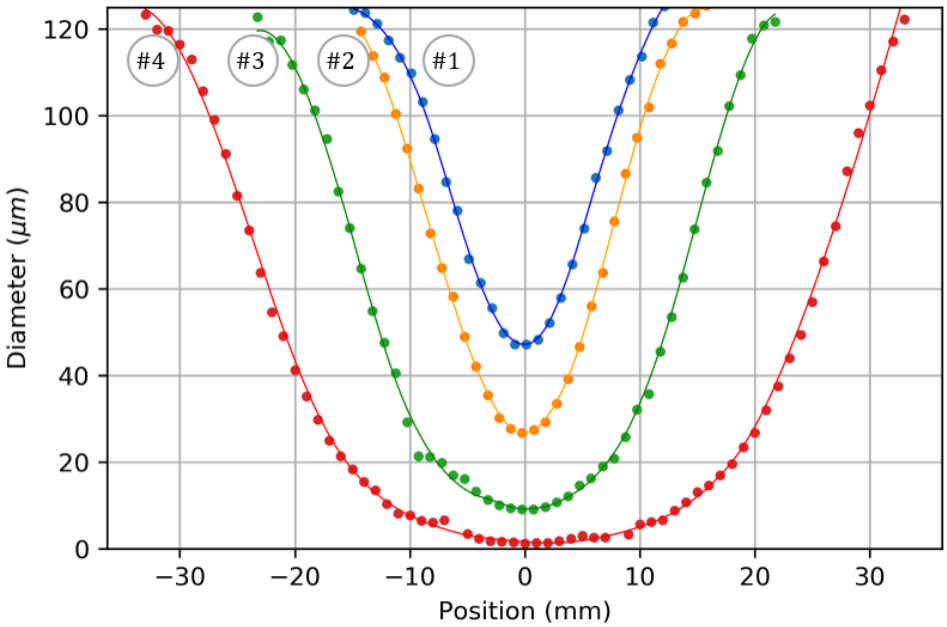

FIGURE 6.8: Profiling of several tapers: $d_w \approx 50, 25, 10, 1.5\ \mu$m.

exist some discontinuity, which may be the result of the fiber hitting the walls of the microheater during pulling and/or removing the microfiber from the microheater.

A summary of the expected (d_{theor}) and measured, by diffraction (d_{diff}) and microscope (d_{micros}), waist diameters can be seen in Table 6.2. The results show good agreement with the theoretical predictions. It is also noticeable that the diffraction method yields values identical to the microscope, with the added advantage of being a contactless method.

Taper	Travel (mm)	d_{theor} (μm)	d_{diff} (μm)	d_{micros} (μm)
#1	6.52	46.24	47.17	47.17
#2	9.93	27.6	26.8	27.9
#3	16.62	9.91	9.08	10.46
#4	27.00	2.06	1.26	1.52

TABLE 6.2: Waist diameter analysis for the tapers represented in Figure 6.8.

6.3 Summary

In this chapter, the geometric properties of the microfibers were analyzed.

The relationship between the waist diameter and the pulling length was found to follow Birks' model for fiber tapering with a *hot-zone* length of 6.6 mm [8]. Considering that the microheater slot has 30 mm, this value is acceptable. However, it was later concluded that L_0 lack physical meaning.

A diffraction experiment for the profiling of the microfibers was set up. The measured diameters were in agreement with the measurements in the optical microscope, with the advantage of being obtained through a contactless method. However, the theoretical model for the diameter profile was found to be lacking, as the *hot-zone* of the microheater is too long. An updated model would have to take into consideration fluid dynamics.

Chapter 7

Light transmission and the Monitoring of the Tapering Process

In Chapters 5 and 6, the fabrication technique and geometric profile of the microfibers were discussed. However, the optical characterization is yet to be performed. This chapter's aim is to provide an analysis of light transmission in the microfibers.

When devising the optical analysis of the microfibers, one option was to simply characterize the microfibers separately on a different setup. In that case, however, only information about the final result—the fabricated microfibers—would be available. Seeing that one of the main goals of this work is the optimization of the tapering process, it made sense to monitor the light transmission during the fabrication. That way it would be easier to supervise the process in real-time and compare the fabricated microfibers with the original fibers. Thus, the experimental setup presented in Chapter 5 was updated with the addition of a light source and a detector, as in Figure 7.1.

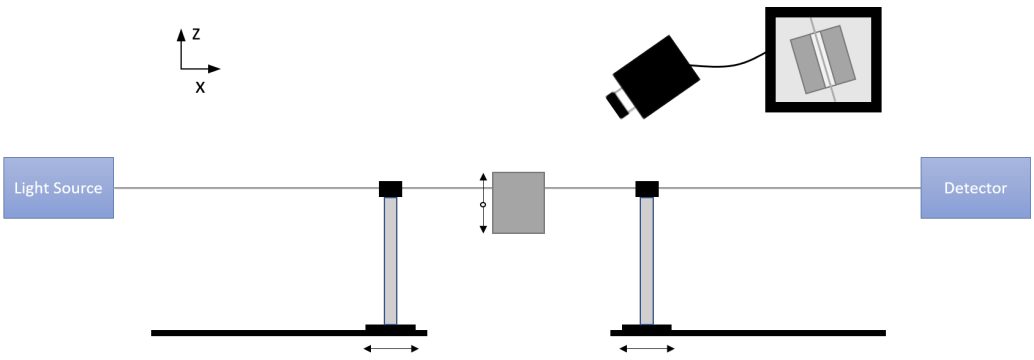

FIGURE 7.1: Tapering setup, updated for the monitoring of the optical transmission.

7.1 Infrared Light

Fiber optic communications is primarily performed in wavelength ranges where optical fibers enjoy low transmission losses, mainly in the near-infrared range. Therefore, to enable the integration in standard fiber optic devices, it is customary to optimize new optical components for this wavelength range, where, generaly, the fiber is single-mode. For this purpose, an C-band light source was used (*Photonetics FIBERWHITE Broadband Erbium-Doped Fiber Source*). The light detection was carried by the *Advantest Q8384* Optical Spectrum Analyzer. The output optical spectrum of a fiber, before pulling, is represented in Figure 7.2.

The fabrication of the microfibers proceeded entirely as described in Chapter 5, with successive optical spectra being recorded and analyzed. For example, Figure 7.3 shows the evolution of the optical transmission T, i.e., the optical power normalized to the starting value, at a single wavelength $\lambda = 1550$ nm, for symmetric pulling at 0.030 mm/s each stage. The transmission evolution exhibits an oscillatory behavior, attributed to interference with modes of the tapered fiber excited during pulling, after which it is approximately constant, with a slight decay as the microfiber decreases in diameter.

The oscillatory behavior is without impact on the transmission of the final microfiber. However, considering the goal of adiabatic microfibers (see Appendix C), no higher-order modes should have been excited. To analyze how this behavior depended on the fabrication parameters, several microfibers where produced at different pulling speeds: 0.010,

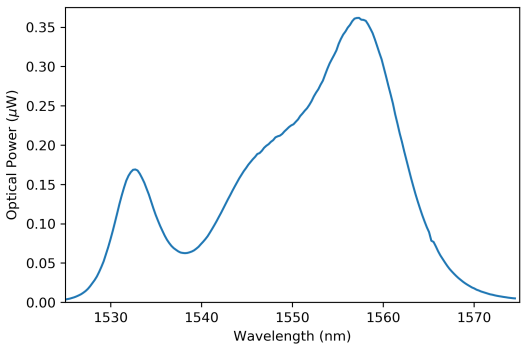

FIGURE 7.2: Optical Spectrum of the C-band optical source, before pulling.

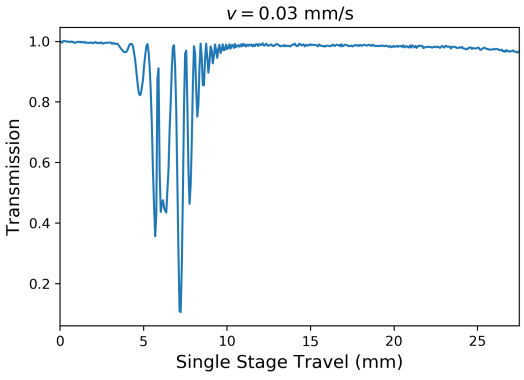

FIGURE 7.3: Transmission monitoring at 1550 nm, during pulling, for a pulling speed of 0.030 mm/s.

0.020, 0.030, 0.050 and 0.075 mm/s; and for the same pulling length. The respective transmission evolutions are plotted in Figure 7.4[6].

The slower the tapering, the better the result. The oscillatory behavior significantly reduces for slower pulling speeds and transmission at the end is higher for these cases. Table 7.1 summarizes the results, T_{min} being the minimum value of transmission and T_{end} the transmission of the finalized microfiber.

Speed (mm/s)	$T_{minimum}$	T_{end}
0.010	0.984	0.992
0.020	0.741	0.995
0.030	0.105	0.933
0.050	0.027	0.906
0.070	0.046	0.862

TABLE 7.1: Transmission dependence on pulling speed, at λ=1550 nm.

It can be concluded that slower pulls result in better microfibers: as there is fewer interference with excited cladding modes (the tapers are 'more adiabatic' for slower pulls), and the optical transmission at the end of the pull is higher.

The model presented in Section 4.1 for the shape of the microfibers concludes that the taper geometry is unrelated to the pulling speeds. Following that logic, the optical transmission should also be independent of the pulling speed. However, as already discussed in Chapter 6, this model is inadequate for the microfibers fabricated in this work. It is possible that for higher pulling speeds, the core to cladding ratio may be irregular, which could explain the resulting oscillations.

To finalize this analysis, the practicality of the speeds still needs to be addressed. In truth, with the current tapering setup, pulling speeds of 0.010 mm/s, are impractical, as it is extremely difficult to remove thinner microfibers ($d < 10$ mm) from the microheater without them hitting the walls and breaking in the process. Since, for 0.020 mm/s this issue ceases to exist, and the overall transmission at the end of pulling is roughly the same, $v = 0.020$ mm/s became a wiser choice. All microfibers presented in this document were, unless stated otherwise, fabricated with pulling speeds of 0.020 mm/s.

[6]Note that the sampling frequency is the same on all attempts, thus the number of data points is lower for higher velocities.

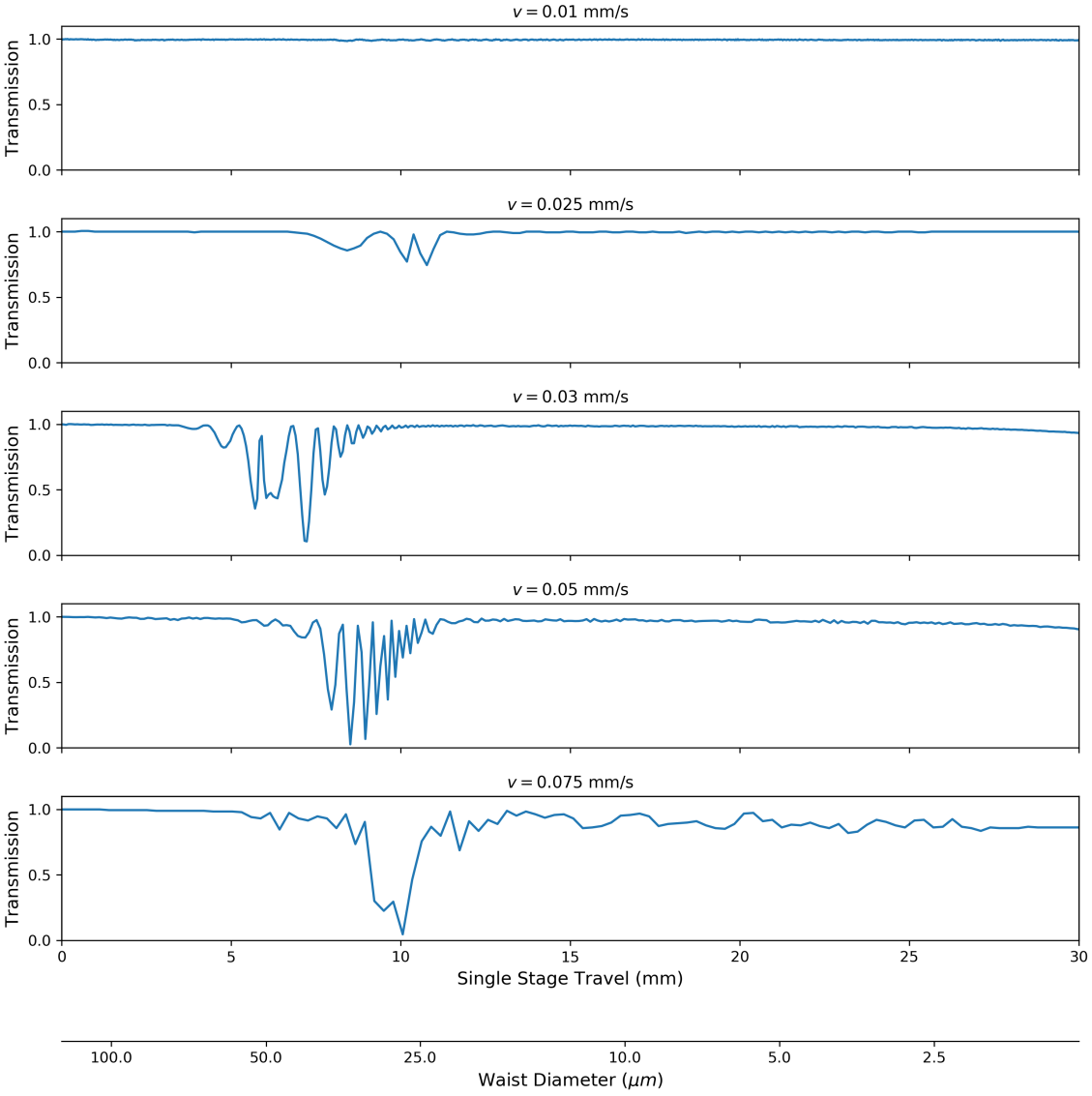

FIGURE 7.4: Transmission monitoring at 1550 nm, during pulling, for various pulling speeds.

7.2 White Light

It is also usual to have optical components working at lower wavelength ranges, namely 488–515 nm, 633 nm, 1064 nm, from Argon, Helium-Neon, and Nd:YAG lasers, respectively; at which the optical fiber is multimode. It is possible to encompass all these ranges utilizing a white-light source. To analyze the optical transmission of the microfibers in the visible spectrum, the *Ocean Optics HL-2000* Halogen Lightsource was used, in cooperation with the *Ocean Optics USB-4000* modular spectrometer. The optical spectra of the light source, before and after a 30 mm single-stage travel pulling, can be accessed in Figure 7.5. This source emits significant power in the 500–1000 nm wavelength range. After pulling, the optical spectrum is severely modified, decreasing drastically in intensity, and showing beat-like oscillations.

The spectra were recorded during pulling. Figure 7.6 plots the evolution of the transmission for several wavelengths[7], which show the same overall evolution. After elongation of about 3mm the intensity starts to strongly oscillate. This is attributed to mode interference. As the taper gets thinner and higher modes stop being guided, this oscillatory behavior decreases in amplitude but increases in frequency, until the transmission reaches a constant state. For even thinner diameters (single stage travel >20 mm), there are occasional drops in intensity. This is attributed to modal cutoff (refer back to Figure 3.2), and can be used to monitor the diameter of a taper [106, 107].

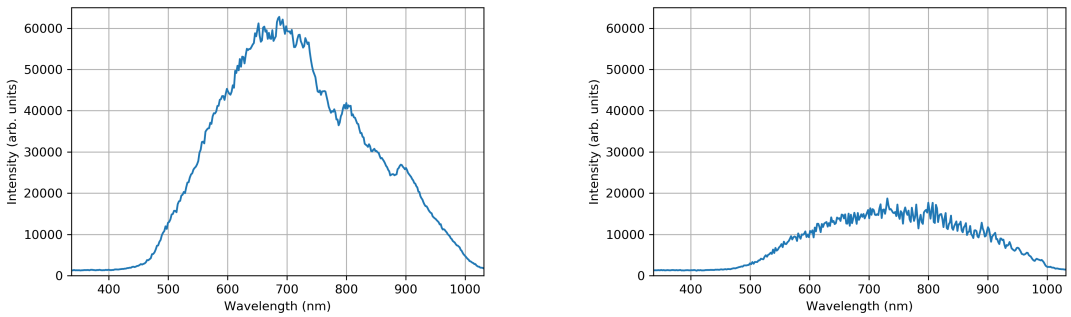

(A) Before (B) After

FIGURE 7.5: Typical optical spectrum of the halogen light source, before and after pulling.

[7]The data refers to the fabrication of a single microfiber, as the entire wavelength range is recorded

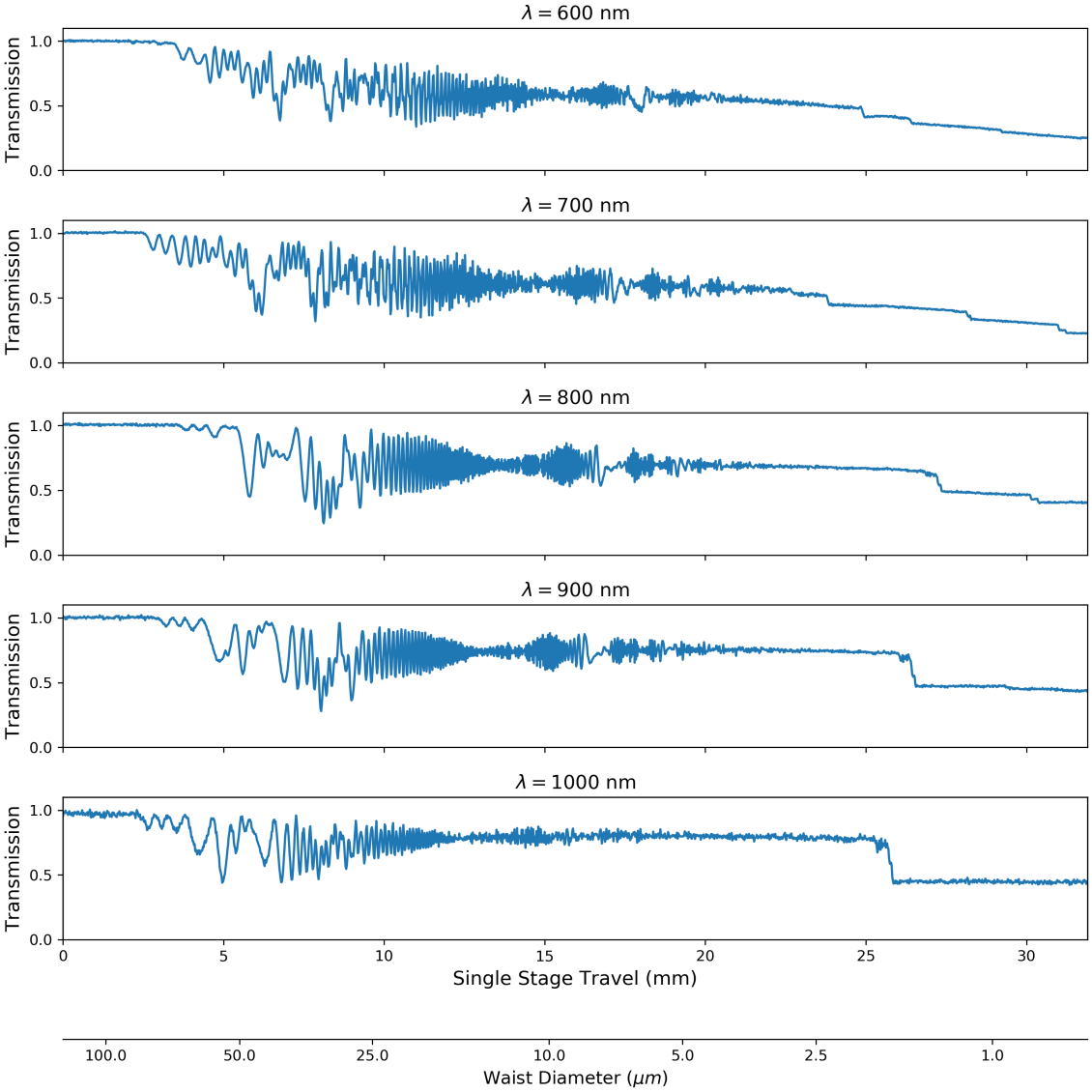

FIGURE 7.6: Transmission monitoring of the white light, during pulling, for selected wavelengths.

7.2.1 Diameter Monitoring due to Modal Cutoff

In this section, an analysis of the intensity drops in the profiles of Figure 7.6 will be performed, in order to monitor and accurately measure the diameter of a microfiber.

Starting with one of those plots, for example at 600 nm wavelength, Figure 7.7 exhibits three discernible drops (circled). In order to determine when they occurred, the profile was smoothed (Figure 7.8, top) and its derivative was calculated and smoothed (Figure 7.8, bottom)). The intensity drops correspond to the minima of the derivative (dashed lines). In this case, the drops occurred at 24.89 mm, 26.40 mm and 29.23 mm single stage travel.

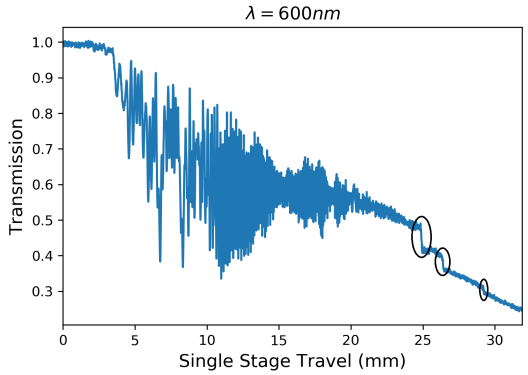

FIGURE 7.7: Transmission, during pulling, at $\lambda = 600$ nm. Visible drops circled

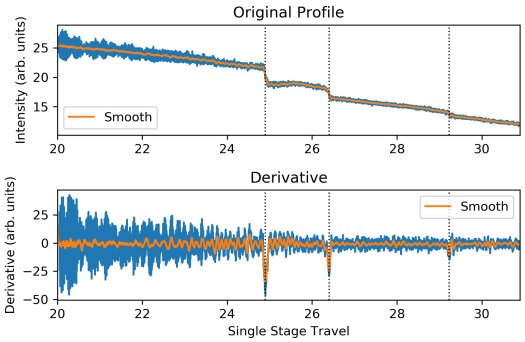

FIGURE 7.8: Profile (top) and its derivative (bottom), with the calculated drop positions as dashed vertical lines

Repeating the analysis to the entire range of the light source—from 500nm to 1000 nm in 20 nm increments—it is possible to relate the wavelength and the location of the drops, as in Figure 7.9.

There seems to be an order to these drops, as they can be easily grouped and their general behavior is the same: a given drop occurs later for smaller wavelengths, resembling a slowly varying exponential decay. This reinforces the idea that this is the result of mode cutoff and not some other exotic property, since for smaller wavelengths a mode is more confined, so its cutoff occurs at a thinner diameter / longer pull. Another thing to notice is that no drop extends to the entire wavelength range, each having a start and end wavelength. The reasoning behind this is that either the mode that suffers cutoff is left unexcited at the wavelength or simply that the intensity drop is so small that it passes unnoticed.

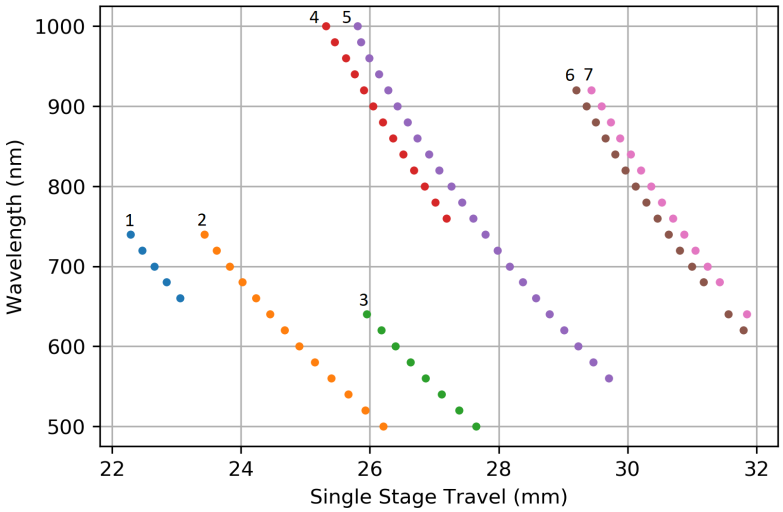

FIGURE 7.9: Wavelength *vs* Pulling Length relationship for the detected intensity drops

The plots of Figure 7.9 can be converted in a way that relates the drops directly to the waist diameter of the microfibers, by recalling the relation between pulling length and waist diameter discussed in Section 6.2.1. This allows to get to the plots of Figure 7.10.

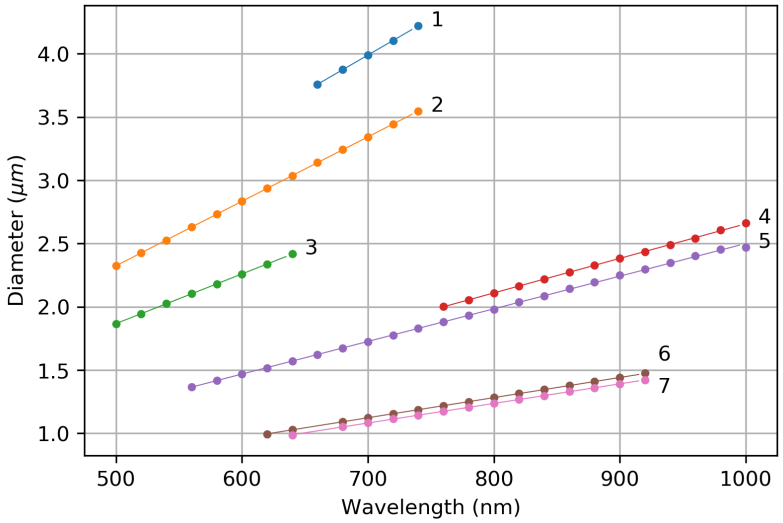

FIGURE 7.10: Diameter *vs* Wavelength relationship for the detected intensity drops, and corresponding linear fits.

The expected diameters for when the drops occur are linearly related to the wavelength. As presented in the theoretical analysis of Section 3.1, it was defined:

$$V = \frac{\pi}{\lambda} d \sqrt{n_1^2 - n_2^2} \tag{7.1}$$

	fit: $d = a\lambda + b$				
Drop #	a (nm/nm)	b (nm)	r^2	λ range (nm)	$V_{calc.}$
1	5.77 ± 0.04	-50 ± 20	0.9998	660–740	18.72
2	5.094 ± 0.006	-223 ± 4	0.99998	500–740	16.53
3	3.924 ± 0.009	-95 ± 5	0.99996	500–640	12.73
4	2.73 ± 0.01	-76 ± 1	0.9998	760–1000	8.86
5	2.58 ± 0.01	-80 ± 9	0.9996	560–1000	8.37
6	1.591 ± 0.003	-9 ± 3	0.99994	620-920	5.16
7	1.547 ± 0.004	-2 ± 4	0.99990	640–940	5.02

TABLE 7.2: Fitting parameters for the intensity drops (Figure 7.10).

Knowing that the cutoffs occur at specific V numbers and ignoring wavelength dependent refractive indices, it comes that $d \propto \lambda$, the proportionality constant being $V/(\pi\sqrt{n_1^2 - n_2^2})$. To check how the curves in Figure 7.10 follow this behavior, they were fitted to the expression of Equation 7.2.

$$d = a\lambda + b \tag{7.2}$$

The fitting parameters are shown in Table 7.2.The drop diameter-response in the wavelength is clearly linear, with all $r^2 \geq 0.9996$. The last column shows the cutoff V numbers calculated from $V_{calc} = a\pi\sqrt{n_1^2 - n_2^2}$, with a the fitted parameter, $n_1 = 1.4377$ and $n_2 = 1$. The V numbers are high, meaning that the drops represent the dissipation of high-order modes. With the last value being 5.02, it suggests that the single-mode region, given by $V < 2.405$, is being approached.

To validate this analysis, three tapers were fabricated, with their optical spectra recorded during pulling. Given the single stage travel (SST), the expected diameter through equation 6.2 was calculated, d_1. Then, the recorded spectra were analyzed to check where, at the time of stopping the pulling, occurred an intensity drop. Using the fitted expression above, d_2 was calculated. Finally, the tapers were processed under the optical microscope in order to measure their waist diameters, $d_{microsc}$. Table 7.3 summarizes the results.

Diameter measuring through modal dissipation is more accurate than by the pulling length. However, while tapers #2 and #3 show errors of less than 2.5%, taper #1 shows a greater error of 24%. This is believed to be a result of the dissipation of a mode yet unrepresented. It seems that a higher-order mode was excited during the fabrication of that specific taper and its dissipation resulted in the intensity drop, thus falling outside any of the previous equations.

	Pulling Length		Mode Cutoff		Microscope
taper	SST (mm)	$d_{(1)}$ (μm)	drop	$d_{(2)}$ (μm)	$d_{microsc}$ (μm)
#1	22.67	3.98	1^{st} @630nm	2.98	3.93
#2	24.51	3.00	1^{st} @524nm	2.44	2.50
#3	26.90	2.09	2^{nd} @680nm	1.67	1.68

	Error	
taper	$d_1 \leftrightarrow d_{microsc}$	$d_2 \leftrightarrow d_{microsc}$
#1	1.2%	24%
#2	20%	2.4%
#3	24%	0.6%

TABLE 7.3: Validation of the fitting expressions for the measurement of waist diameter by modal dissipation.

7.2.1.1 White Light: Final Regards

It is possible to measure the diameter of the microfiber considering the intensity drops due to modal dissipation.

A further step, neglected for the time being, is the fabrication of tapers with specific waist diameters. This could be done by setting the desired diameter before pulling and using the expressions above to relate that with an intensity drop. By monitoring the transmission in real time, and at the right wavelength, it could be possible to stop the pulling precisely when the drop occurs. This is yet to be tried as there is still a degree of user interference (the stopping of the pull should be decided by the user, immediately after the right drop occurs) that could lead to error, since some drops are easier to discern than others.

To finalize this discussion, there is still something to say about one specific step of this analysis. In order to go from pulling length to diameter—from Figure 7.9 to Figure 7.10—, the relation discussed in Section 6.2.1 was used. The question is: is it valid to do that? What if the exponential relationship between the pulling length and the diameter, as fitted, is inadequate for thinner diameters: then, the conclusions of this section should surely suffer from those errors. Or even, what if, during the tapering of the fiber whose spectra has been analyzed, the fiber had slipped in the clamps: in that case the relation between pulling length and diameter should be somehow different—translated, for instance—. The rebut of the first example is present in Table 7.2: since the values of r^2 for the linear regression are so high it seems that the exponential decay does, in fact, hold for thinner diameters; otherwise, surely, the agreement with the theory ($d \propto \lambda$) would be weaker. As for the second argument: yes, slipping of the fiber could have heavily affected

the results, but the low errors shown on Table 7.3 suggest otherwise; or at least that the introduced errors are minor.

Being this a first foray into this delicate area, and given the short time available to explore further methods and techniques, this analysis presents a good first step.

7.3 Summary

Light transmission monitoring during the fabrication of the microfibers provided a real-time check on the tapering process and allowed for its optimization and for the experimental observation of some properties of light propagation in microwires, as discussed in Chapter 3.

In the infrared C-band around 1550 nm, at which the untapered fiber is single-mode, the fabricated microfibers showed low loss ($\sim$ 0.14% on the worst case for an expected 1.3 μm waist diameter microfiber), but the transmission evolution was found to depend on the pulling speed. Analyzing pulling speeds of 0.01, 0.020, 0.030, 0.050 and 0.075 mm/s it was found that both the oscillatory behavior due to interference with cladding modes and the final transmission clearly decreased for slower pulls. However, as it would be impractical to keep making tapers at 0.01mm/s, all the tapers presented during this work were fabricated with pulling speeds of 0.02 mm/s.

As for white light monitoring: at this wavelength range the untapered fiber is multi-mode. Therefore, the transmission evolution was heavily affected by modal interference. As the taper diameter decreases, the transmission profile shows occasional intensity drops due to modal cutoff. A method to monitor the microfibers diameter using this particularity was developed. However, some further work still needs to be done in this regard.

Chapter 8

Microfiber Response to External Physical Parameters

Optical microfibers can be integrated into devices for a wide range of applications. In particular, due to their properties, such as large evanescent fields, ultra-fast response time, biological compatibility, and small footprint, optical microfibers have been developed into a myriad of sensors for physical, chemical and biological phenomena.

Optical sensing in microfibers is a result of the large evanescent fields. Since optical microfibers can have a large fraction of power outside their physical boundaries, any change to the surrounding environment is echoed in the transmission properties of the light. These changes may occur due to variations in temperature, refractive index, or due to the presence of some chemical or biological species. Several microfiber-based sensor architectures have been reported (see Chapter 2). These include Mach-Zehnder interferometers [67], microfibers with Bragg Grattings [108], and microfiber couplers [57]. Resonant structures such as loops and coils have also been used [109]. In order to increase the overall sensitivity, microfiber-based sensors are often functionalized: coated with specific compounds with a greater response to the desired physical effect and/or chemical substance [48, 62].

In this Chapter, the simplest microfiber device—the uncoated, as-pulled microfiber—will be explored. Therefore, in the following pages, the behavior of optical microfibers when subject to temperature, refractive index, and strain variation will be reported. This will serve both as characterization of the fabricated optical microfibers and to showcase simple possible sensing applications.

8.1 Microfiber Response to Temperature Variation

Fiber optics temperature sensors have been employed in a wide range of applications, in the fields of medicine, environmental health and safety, and cryogenics, among others. Owing to their light-weight, small size, flexibility, durability under harsh conditions and immunity to electromagnetic interference, optical fiber temperature sensors can provide both low- and high-temperature sensing, with high sensitivity, and fast response.

A wide variety of microfiber-based temperature sensors have been proposed [110], both in non-resonant—with couplers [42], gratings [111] and interferometers [112]—and resonant—like knots [113]—configurations. However, no uncoated, as-drawn microfiber sensor has been accomplished. Due to the low thermo-optic effect on undoped silica glass, straight microfibers are passive structures and need to be coated for temperature sensing.

8.1.1 Theoretical Background

When an optical material is subject to a temperature change, two separate phenomena can occur. These are thermal expansion and the thermo-optic effect.

Thermal expansion corresponds to the change of the volume of a material in response to the temperature. This occurs because,with the heat, the molecules increase their kinetic energy, vibrate more and create a greater average separation with their neighboring molecules, expanding. This effect is described by the coefficient of thermal expansion, α_V. In an optical fiber it is usual to consider the linear coefficient of thermal expansion, α_L, that is the fractional change in length per degree of temperature change:

$$\alpha_L = \frac{1}{L}\frac{dL}{dT} \tag{8.1}$$

In fused silica optical fibers, a typical value for thermal expansion is $\alpha_L \approx 5.5 \times 10^{-7}(/\mathrm{K})$.

The thermo-optic effect is related to the refractive index variation with temperature and can be mathematically equated as:

$$n = n_0\left(1 + \alpha_1 T + \alpha_2 T^2 + \alpha_3 T^3 + \cdots\right) \tag{8.2}$$

where n_0 is the refractive index at 0 °C and α_1, α_2 and α_3 are the first-, second- and third-order thermo-optic coefficients. For a standard single-mode fiber, the thermo-optic coefficient increases approximately linearly with the temperature: $n = n_0\left(1 + 5.327 \times 10^{-6} T\right)$, in the temperature range [20–400] °C, for $\lambda \approx 1.55$ μm [114].

Considering that in an optical microfiber part of the propagating light travels in the evanescent field, its transmission spectrum is also affected by the change of the surrounding environment's refractive index due to the temperature change (the thermo-optic effect for the surrounding environment). For air, this effect changes the refractive index in the 10^{-5} order [115]. The wavelength-dependent thermo-optic effect in water can be seen in Appendix E.

In a microfiber, all these temperature-based effects affect the optical path of the propagating light. On a multimode wavelength region, changes to the optical path reflect themselves as changes to the phase difference between interfering modes, which may result in wavelength shift of the interference pattern.

8.1.2 Air-clad Microfibers

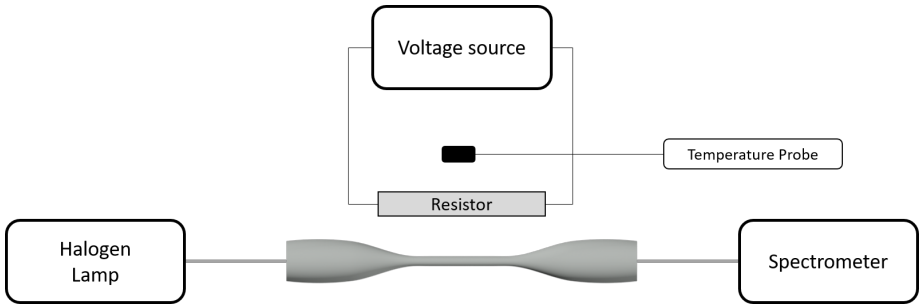

FIGURE 8.1: Experimental setup for temperature measurements in air.

The experimental setup for the analysis of the microfibers' transmission response to temperature is depicted in Figure 8.1. The resistive element (an aluminum housed, 50 W, 10 Ω resistor), powered by a voltage source (up to 15 V), dissipates energy through Joule effect and heats the optical microfiber, that is located about 2mm away. On the opposite side of the resistor, at the same distance, a thermometer is placed to record the local temperature. The setup is complemented with the optical components: the *Ocean Optics* Halogen Light-source *HL-2000* (λ from 400 nm to 100 nm) and the *Ocean Optics USB-4000* modular spectrometer.

The resistor is powered until the thermometer reads a temperature of about 60 °C, at which point the voltage source is turned off. The optical spectra of the microfiber and the temperature are automatically recorded during cooling.

The experiment was performed on two microfibers, with waist diameters of, approximately, 10 μm and 6 μm. The evolution of the optical transmission due to temperature variations is represented in Figure 8.2. The data is zoomed-in in the wavelength range

around 633 nm and shows the transmission peaks normalized to the spectrum's baseline (refer back to Figure 7.5 to see an example of the entire spectrum). The main effect of temperature on the optical spectrum is shown by a small blue-shift. Despite the transmission peaks shifting to lower wavelengths, their maximum power remained roughly the same on the entire temperature range, meaning no additional loss occurred due to temperature.

Plots, and respective linear fits, for some transmission peaks from Figure 8.2 are shown in Figure 8.3. The fitting constants can be seen in Table 8.1. In fact, the peak shift evolution is roughly linear with temperature, although the r^2 values could possibly be improved if the spectrometer had a greater resolution. As for the sensibility, it is of the order of 100 pm/°C, averaging -125 pm/°C for the 10 μm microfiber, and -98.2 pm/°C in the 5 μm one. The fact that temperature sensitivity is higher for the 10 μm microfiber indicates that the prominent phenomena are the internal ones, meaning that the thermal expansion and thermo-optic effect on the microfiber. As expected, air temperature variation, in the analyzed range, has small effect on the transmission of the air-clad uncoated optical microfibers. For reference, functionalized microfiber temperature sensors have been reported with much higher sensitivities. Xue *et al.* demonstrated an isopropanol-sealed optical microfiber taper in a capillary with a sensitivity of 3.88 nm/°C over the 20–50 °C range [116]. An Al_2O_3 nanofilm coated microfiber interferometer with 2.44 nm/°C sensitivity over a greater range, 20–120 °C, has been reported [117].

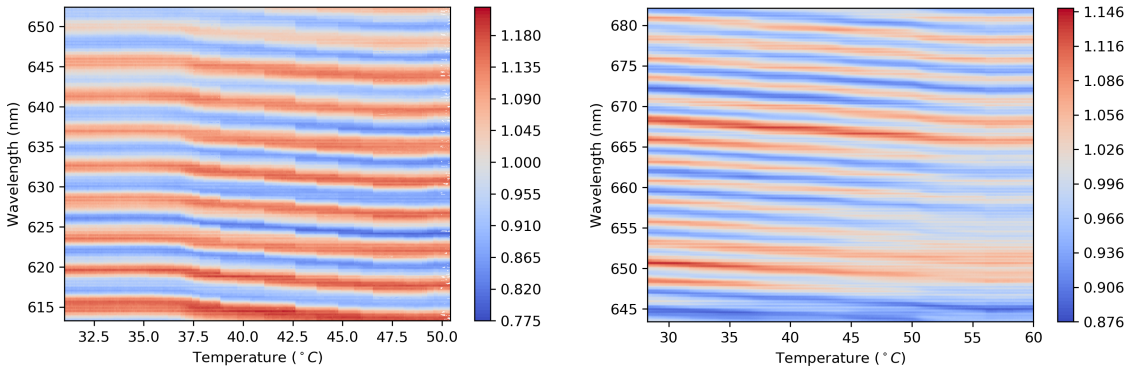

(A) $d = 10\mu$m (B) $d = 6\mu$m

FIGURE 8.2: Optical transmission dependence on the temperature for microfibers with 10μm and 6μm waist diameters.

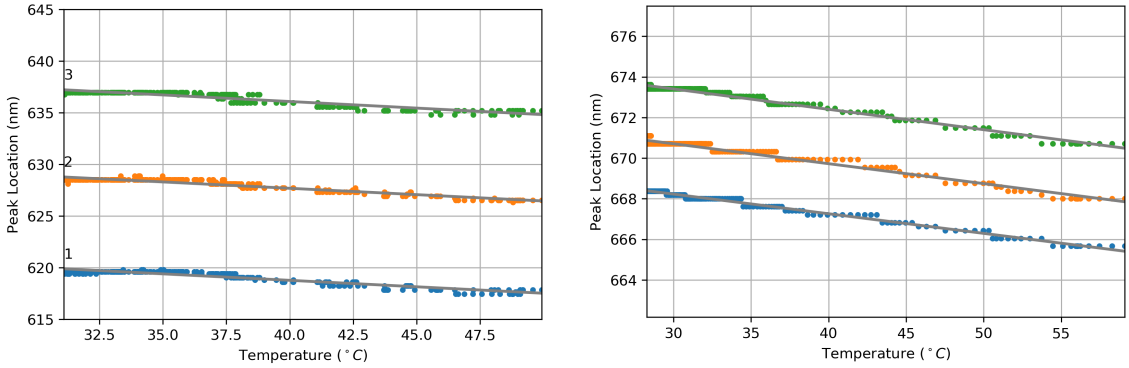

(A) $d = 10\mu$m (B) $d = 6\mu$m

FIGURE 8.3: Plot, and linear regression fit, for the evolution of the peaks of the optical transmission in response to temperature, for microfibers with 10μm (left) and 6μm (right) waist diameters.

		fit: $y = ax + b$		
Fiber	Peak	a (pm/°C)	b (nm)	r^2
10μm	#1	-125 ± 2	623.8 ± 0.1	0.89
	#2	-123 ± 2	632.61 ± 0.08	0.92
	#3	-127 ± 3	641.2 ± 0.1	0.88
6μm	#1	-96.6 ± 0.7	671.12 ± 0.02	0.99
	#2	-98 ± 1	673.65 ± 0.04	0.97
	#3	-100 ± 1	676.41 ± 0.03	0.98

TABLE 8.1: Temperature dependent peak shifts, in air: fitting parameters.

8.1.3 Water-clad Microfibers

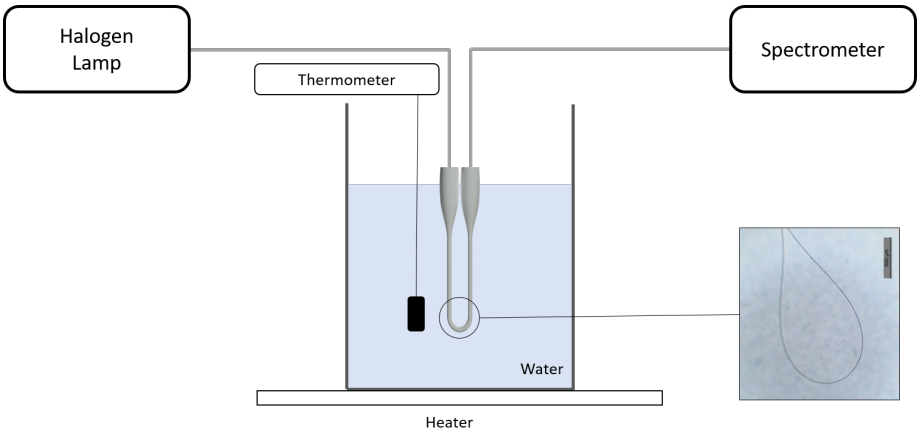

FIGURE 8.4: Experimental setup for temperature measurements in water.

In order to investigate the temperature dependence on the transmission spectrum of water-clad microfibers, a different experiment was developed (Figure 8.4). A metallic basin was filled with water and placed on top of an electric heater. When the water reached its boiling point, the heater was turned off, and the recipient was left to cool unaided. After waiting for the water turbulence to reduce, at about 80 °C, the microfiber was inserted and its optical spectrum was recorded over time until the water cooled down to room temperature. As usual, the optical components are the *Ocean Optics* Halogen Light-source *HL-2000* (λ from 400 nm to 100 nm) and the *Ocean Optics USB-4000* modular spectrometer. This time, a digital thermometer was used. Therefore, the temperature was recorded manually and at irregular intervals. In order to attribute a temperature to the spectral data, over time, an interpolation was made. It was observed that the water temperature during the cooling cycle followed an exponential decay.

The experiment was performed on microfibers with waist diameters of, approximately, 10 μm and 5 μm in a bent configuration, as in Figure 8.4 (bending measurements can be seen in Appendix D). The evolution of the optical transmission with temperature is represented in Figure 8.5. In opposition to the behavior on an air-clad microfiber, the spectral shift was undetected, meaning that the thermal expansion of the microfiber and thermo-optic effects on water are balanced. Therefore, the main effect of temperature on the optical spectrum is on the transmitted power. Figure 8.6 shows the optical power dependence on temperature for $\lambda = 633$ nm wavelength for the 10 μm and 5 μm diameter microfibers. Although the 10 μm microfiber shows a greater variance, the 5 μm is more affected by the temperature variation, as its maximum loss is 26% compared to the 13% on the other case.

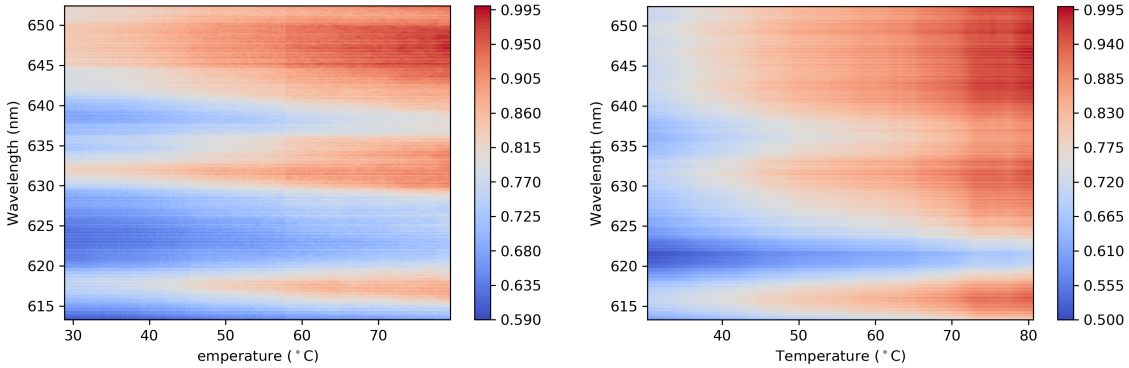

(A) $d = 10\ \mu$m (B) $d = 5\ \mu$m

FIGURE 8.5: Optical transmission dependence on the temperature for microfibers with 10μm and 5μm waist diameters.

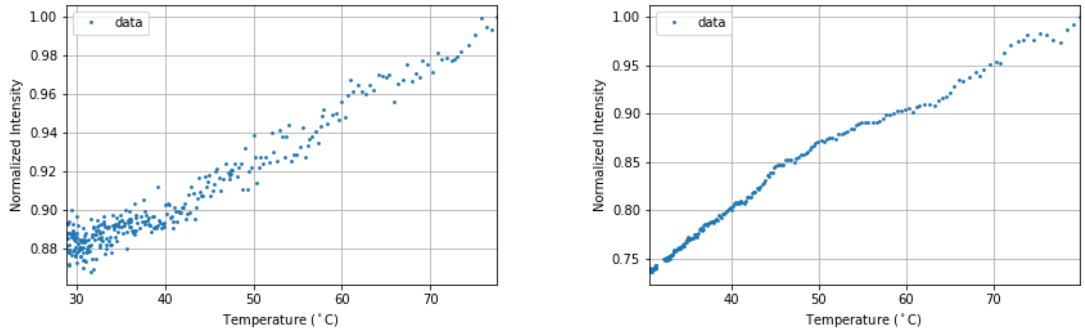

(A) $d = 10\ \mu$m (B) $d = 5\ \mu$m

FIGURE 8.6: Optical transmission dependence on the temperature for microfibers with 10μm and 5μm waist diameters, at $\lambda = 633$ nm.

This is due to the fact that, in a water-clad microfiber subject to temperature variation, the predominant effect is the thermo-optic effect in water. Since the 5 μm microfiber has more power in the evanescent field, it is natural that it gets affected more.

The transmitted power grows with the temperature. Considering that the refractive index of water decreases with the temperature (see Appendix E), the index contrast between glass and water increases. As the confinement is greater for higher index contrasts (see Figure 3.5), it makes sense for the transmitted power to increase with the temperature.

8.1.3.1 Transmission dependence on the Refractive Index

The transmission dependence on temperature is mainly the result of the thermo-optic effect in the water, as the microfiber senses the water refractive index. As discussed in Chapter 3, the optical properties of microfibers are profoundly affected by the refractive

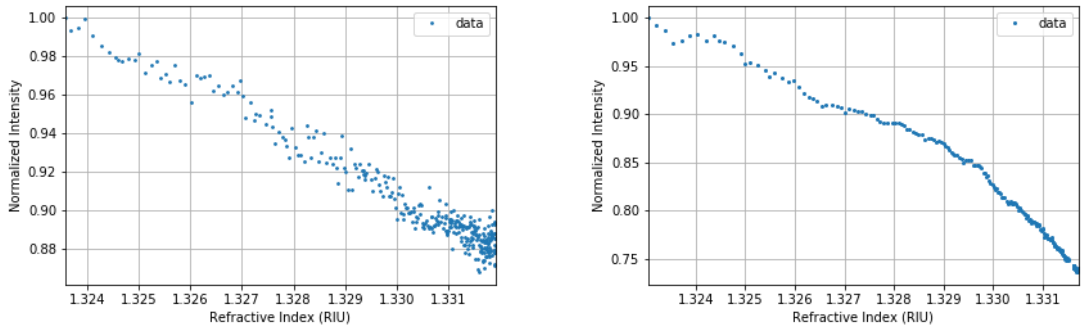

(A) $d = 10\ \mu$m (B) $d = 5\ \mu$m

FIGURE 8.7: Transmission dependence on the refractive index for microfibers with 10μm and 5μm waist diameters, at $\lambda = 633$ nm.

index of the surrounding medium, which makes microfibers suitable for application as refractive index sensors. So far, several microfiber-based refractive index sensors, especially for microfluidics applications, have been developed [118].

The analysis of the dependence of the optical transmission on the refractive index can be performed considering the general equation for the refractive index of water with temperature, as seen in Appendix E. With this information, it is possible to plot the relationship between the transmission and the water refractive index (Figure 8.7). Looking back to Figure 8.6, the general behavior is as expected, since the temperature→refractive index transformation is approximately linear in the 30–80 °C range. The optical transmission clearly depends on the refractive index. This showcases the utility of microfibers as refractive index sensors.

8.2 Microfiber Response to Strain

Strain (ϵ) is a dimensionless quantity that gives the amount of deformation per unit length of an object when a load is applied. It is calculated as the quotient between the total deformation (ΔL) and the original length (L):

$$\epsilon = \frac{\Delta L}{L} \tag{8.3}$$

Strain sensing is often performed in civil engineering for building evaluation and in heavy industrial assets, as pipelines, and machinery monitoring. The most commonly used optical fiber strain sensors monitor the peak shift of Bragg Gratings due to fiber elongation. However, some microfiber-based strain sensors have been proposed [56, 119, 120].

In optical microfibers, strain sensing is possible due to the optical path variation with the elongation. Changes to the optical path lead to changes in the phase difference between interfering modes, resulting in a wavelength shift of the transmission spectrum.

The experimental setup for strain measurements is schematized in Figure 8.8. The microfiber was fixed on both ends: one end was glued into a static block while the other was glued into a manual linear stage, with the distance between the fixing points approximately $L = 200$ mm, initially. The stage was moved in 10 μm increments, with an optical spectrum being recorded at each increment. Again, the *Ocean Optics Halogen Lightsource HL-2000* and the *Ocean Optics USB-4000 modular spectrometer* were used.

The optical transmission evolution with strain for the 10μm and 5μm microfibers is represented in Figure 8.9. The loss due to the strain is insignificant. In fact, the main effect of strain in the optical spectra is the spectral shift. Figure 8.10 plots the wavelength 'location' of some peaks. These values were obtained numerically: each recorded spectrum was smoothed and their maximum values were calculated automatically using a python sequence.

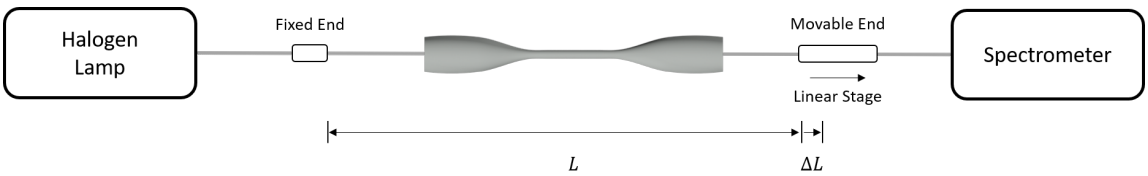

FIGURE 8.8: Experimental setup for strain measurements.

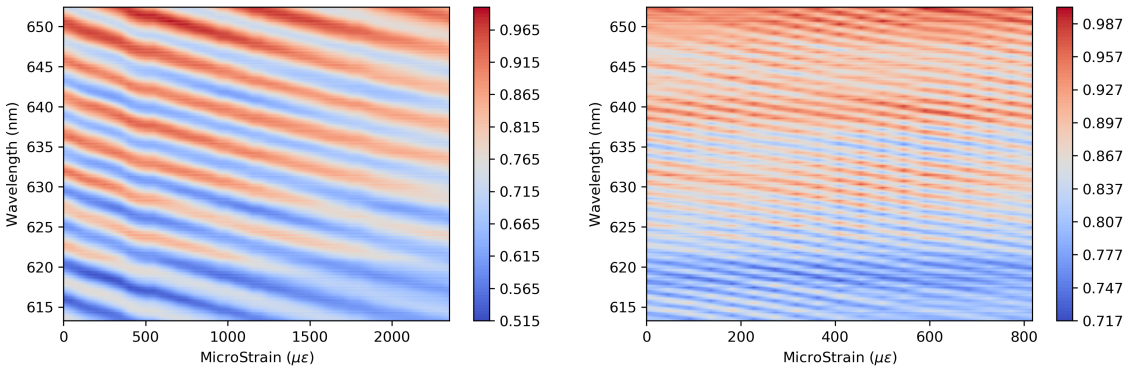

(A) $d = 10\mu$m (B) $d = 5\mu$m

FIGURE 8.9: Evolution of the optical spectrum, centered at $\lambda = 633$nm, as a function of the strain, for microfibers with 10μm(left) and 5μm (right) waist diameters.

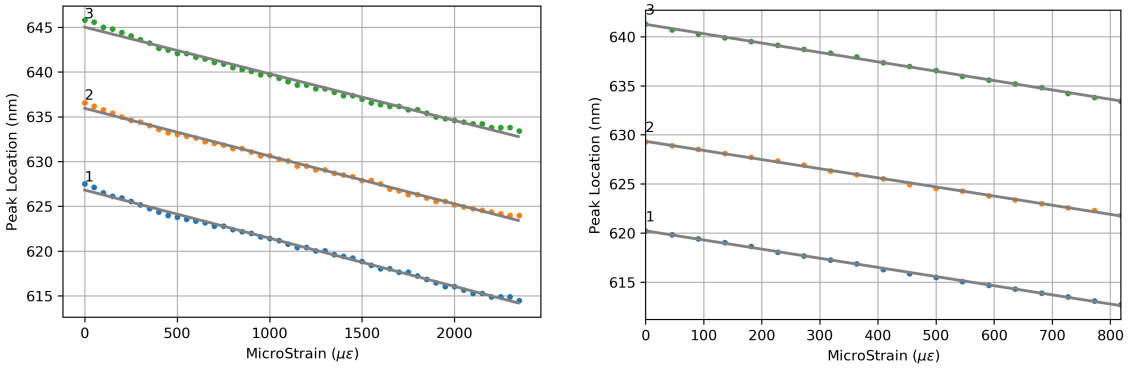

(A) $d = 10\mu$m (B) $d = 5\mu$m

FIGURE 8.10: Plot, and linear regression fit, for some peaks of the optical transmission, for microfibers with 10μm (left) and 5μm (right) waist diameters

		fit: $y = ax + b$		
Fiber	Peak	a (pm/$\mu\epsilon$)	b (nm)	r^2
10μm	#1	-5.38 ± 0.05	626.81 ± 0.06	0.996
	#2	-5.34 ± 0.05	635.94 ± 0.06	0.996
	#3	-5.21 ± 0.07	645.0 ± 0.1	0.991
5μm	#1	-9.32 ± 0.07	620.21 ± 0.03	0.9991
	#2	-9.30 ± 0.07	629.33 ± 0.04	0.9990
	#3	-9.55 ± 0.05	641.25 ± 0.03	0.9990

TABLE 8.2: Peak shift due to strain: fitting parameters.

With the increasing strain, the spectra are blue-shifted. Furthermore, the peak location dependence on the strain seems linear, which is of great importance when designing sensors. In fact, fitting the data to a linear function ($y = ax + b$) gives good results, as shown in Table 8.2. The analyzed microfibers can be used to accurately measure strain, with sensitivities of -5 pm/$\mu\epsilon$ and -10 pm/$\mu\epsilon$, for the 10 μm and 5 μm, respectively. These values are in agreement with the ones by Li *et al.* [56].

8.3 Summary

The optical response of the microfiber to external phenomena is what allows the use of microfibers as sensors. Usually, microfiber-based sensors rely on functional coatings and architectures, such as Mach-Zehnder interferometers, Bragg gratings and couplers to improve the sensitivity. In this Chapter, the response of the uncoated, as-drawn microfibers (with 10 μm and 5 μm diameter) to temperature and strain was analyzed.

When air-clad, the microfibers showed response to the temperature of about 100 pm/°C over the 30–60 °C temperature range. This value is 30–40 times lower than those of functionalized microfibers reported in literature. Power variation (loss) due to temperature was insignificant.

The water-clad microfibers were more affected by the temperature, but only power-wise, as no spectral shift occurred due to a balance between the thermo-optic and thermal expansion effects. Considering the thermo-optic effect on water, the optical transmission was related to the refractive index of the water, demonstrating the microfibers' capacity for refractive index sensing.

Strain sensing was also tested. The optical transmission spectra suffered a blue-shift due to the elongation. Sensitivities were -5 pm/$\mu\epsilon$ and -10 pm/$\mu\epsilon$, for the 10 μm and 5 μm, respectively. These values are compatible with the ones reported by Li *et al.* in 2014 [56].

Chapter 9

Concluding Remarks

The work developed in this dissertation concerned the fabrication and characterization of optical microfibers. It involved extensive literature research, varied numerical simulations, and long hours in the laboratory, either fabricating microfibers, optimizing the setup, designing experiments, or merely sorting through and analyzing the experimental data. All these different aspects have found their way into this document.

Chapter 2 displayed an overview of the published literature on this topic, introducing important concepts and overall describing the standard fabrication methods and typical applications of the microfibers.

The following two chapters, 3 and 4, delved into the theoretical analysis of microfibers. The former described how light propagates in optical microwires, focusing, in particular, on modal propagation, power distribution, and confinement; the topics of nonlinear effects and waveguide dispersion were also considered. The latter presented a simple model for the shape of fiber tapers, introduced the concept of adiabaticity and described the modal evolution along the length of a taper.

The description of the experimental work began in Chapter 5, which depicted the fabrication of the microfibers by enumerating and commenting on the tapering setup and its main components, and detailing the tapering process and posterior handling of the microfibers.

From the fabrication of the microfibers, the focus changed to their characterization. In Chapter 6 the shape of the microfibers was analyzed. The dependence of the waist diameter on the pulling length was found to follow the theoretical model. A diffraction apparatus for the contactless measurement of the microfiber's profile was assembled. This time, the theoretical model was at fault due to neglecting fluid dynamics.

Chapter 7 analyzed the optical transmission of the microfibers during the fabrication process. At the telecommunications band (around 1550 nm), the microfibers were found to have low losses. Some microfibers were fabricated with different pulling speeds, leading to the conclusion that the slower the pull the better the result. White light monitoring showed modal interference and modal cutoff through intensity drops. This peculiarity allowed for the development of a method for the precise measurement of the microfibers waist for diameters smaller than 5μm.

Finally, in Chapter 8, the microfibers' response to external conditions was analyzed. Temperature, both in air and in water, and strain experiments were performed in microfibers with approximately 10μm and 5μm waist diameter. Air-clad microfibers showed sensitivities of about 100 pm/°C over the 30–60 °C range. In water-clad microfibers, spectral shift was irrelevant, however, the optical intensity increased with the temperature. Considering the thermo-optic effect in water, it was showed that the microfibers can sense refractive index variations. In strain sensing, the microfibers showed shifts of -5 pm/$\mu\epsilon$ and -10 pm/$\mu\epsilon$ for the 10 μm and 5 μm, respectively.

9.1 Future Work

This work presents itself as a first foray into the topic at hand and, as such, should not be taken as a finished business. In fact, its inevitable comparison with the work of other research groups as presented throughout this document and in the various references leads to the conclusion that there is still much room for improvement. Thus, future work should be developed with the aim of reaching the so desirable nanoscale and to allow for the incorporation of the microfibers to different fields and applications. To achieve those results some topics could be addressed, including:

- Revising the alignment of the clamps and microheater slot. This was the main setback of this rig, and the reason why microfibers below 1μm were unobtainable. Steps like the addition of grooves for better fiber alignment or even elevating the pulling stages to the height of the microheater could be considered.

- Condensing all computerized input into a single program. The microheater, stage and monitoring control programs are uncoordinated, making the fabrication of the microfibers a complex and somewhat confusing process.

- Playing with the different fabrication variables, like the microheater temperature and the pulling speeds. Accelerating stages may lead to interesting results.
- Overall further optimizing the tapering apparatus, with the inclusion of:
  - Load cells positioned in the clamps, to monitor and prevent fiber slipping, and better relate it with the microheater temperature, fiber viscosity and pulling speeds.
  - A motorized stage to move the microheater along the fiber and allow for the fabrication of microfibers with different profiles and, namely, longer waists.

Appendix A

The Electrical Microheater: Further Information

A.1 Temperature Calibration Chart

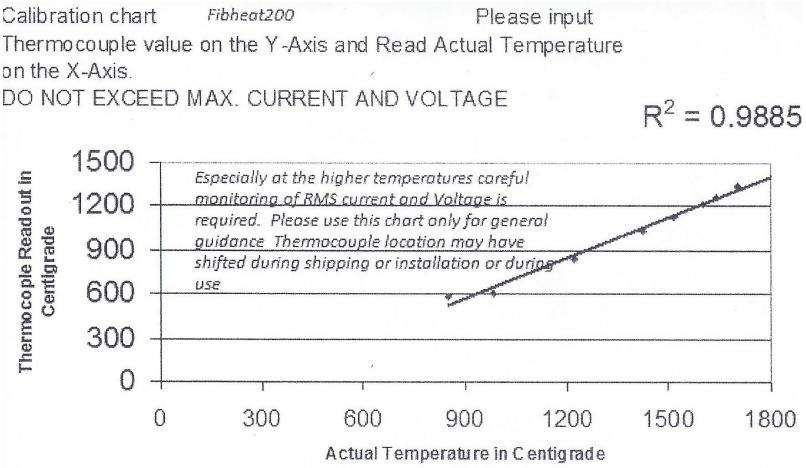

FIGURE A.1: Calibration chart for actual temperature calculations (provided in the FibHeat200 User Manual).

A.2 Electrical Specifications

Max. Temperature	1800°C
Voltage of operation	120V $\rightarrow$ 4V 50/60 Hz
Max. Amps.	2A $\rightarrow$ 75A
Max. Watts	250W

TABLE A.1: Electrical specifications of the FibHeat200 microheater.

Appendix B

Taper Holder: Technical Drawing

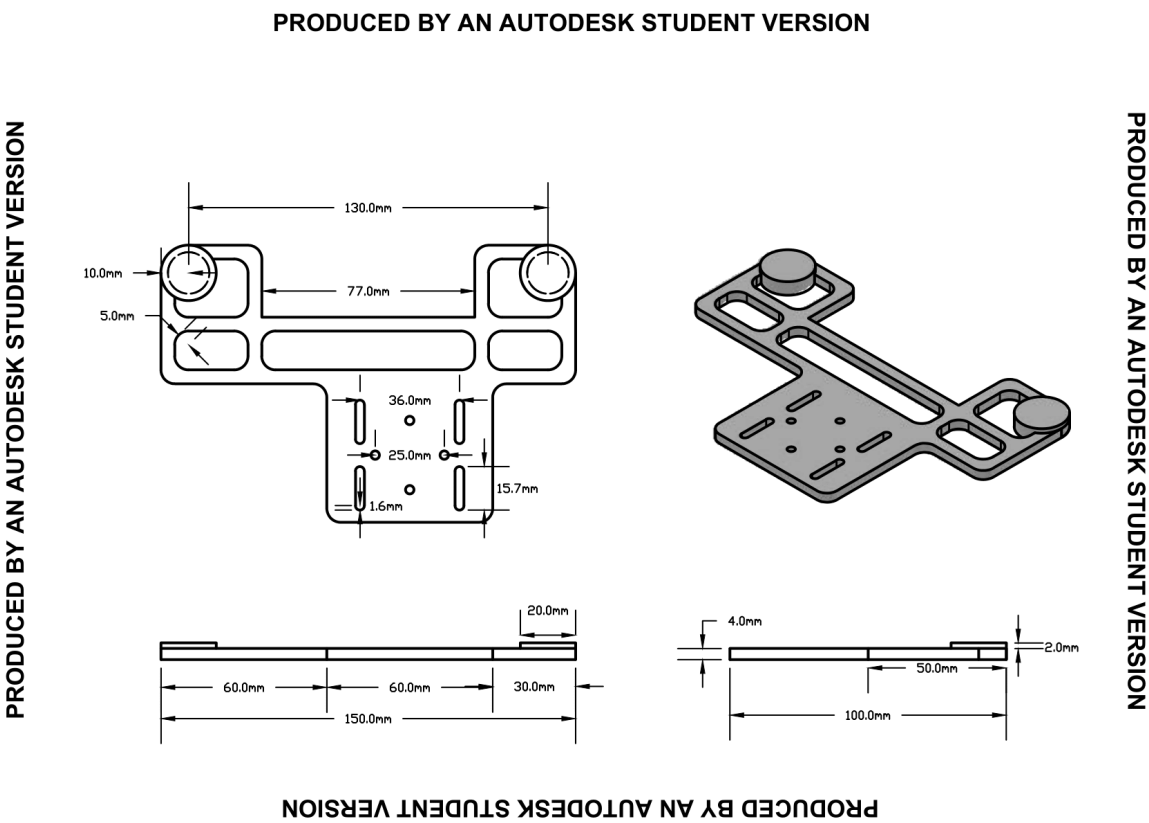

FIGURE B.1: Technical drawing ofa version of the Taper Holder.

Appendix C

Adiabaticity of a Fiber Taper

The adiabaticity can be considered a quality factor of a taper. A taper is considered adiabatic for a given propagating mode when there is no power transfer (coupling) to higher modes. Considering two modes with propagation constants β_1 and β_2 (see the modal propagation analysis in Chapter 3), their beat length, z_b, is defined as:

$$z_b = \frac{2\pi}{\beta_1 - \beta_2} \tag{C.1}$$

When the beat length is long, the two propagation constants are similar, meaning that the modes have approximately the same phase and are very sensitive to changes along the fiber. Thus, non-adiabatic coupling is most likely to occur in this case. Due to symmetry considerations, a mode will only couple to modes with the same circular symmetry [121].

The adiabaticity is directly related to the taper profile. Any taper profile can be described by the angle $\Omega(z)$:

$$\Omega(z) = \left| \frac{\partial r_{\mathrm{co}}(z)}{\partial z} \right| \tag{C.2}$$

where r_{co} is the local radius of the core of the tapered fiber. For smooth transition regions Ω can be approximated to Equation C.3

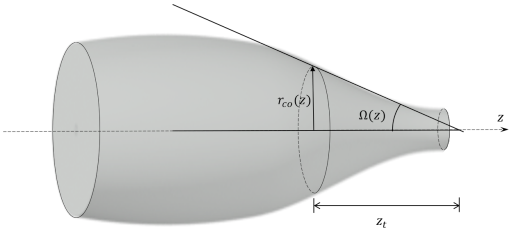

FIGURE C.1: Taper Angle $\Omega(z)$.

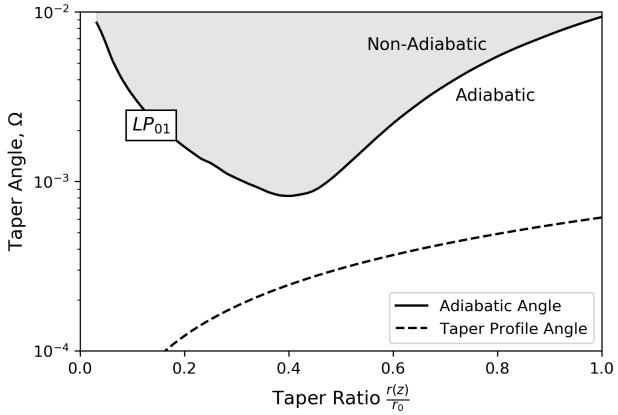

FIGURE C.2: Adiabaticity of the LP01 mode at 1550nm wavelength on an exponential-profile taper.

$$\Omega(z) = \tan^{-1}\left(r(z)/z_t\right) \approx r(z)/z_t \tag{C.3}$$

with z_t the local taper length. To ensure minimal coupling, it is usual to set the limit $z_t = z_b$. Thus, for a transition to be adiabatic it is necessary that $z_t \gg z_b$. Hence, the so called adiabatic angle is given by [121]:

$$\overline{\Omega}(z) = \frac{r(z)\left(\beta_1 - \beta_2\right)}{2\pi} \tag{C.4}$$

with $r = r(z)$, $\beta_1 = \beta_1(z)$ and $\beta_2 = \beta_2(z)$ are being local quantities. If at any point z the taper angle is greater than the adiabatic angle, $\Omega(z) > \overline{\Omega}(z)$, then the taper is non-adiabatic and coupling between modes occurs. Figure C.2 shows the adiabatic angle for the LP01 mode (the fundamental mode) at 1550nm wavelength, and the taper angle corresponding to an exponential taper. This kind of taper is adiabatic for the fundamental mode at 1550 nm.

Appendix D

Microfiber Bending

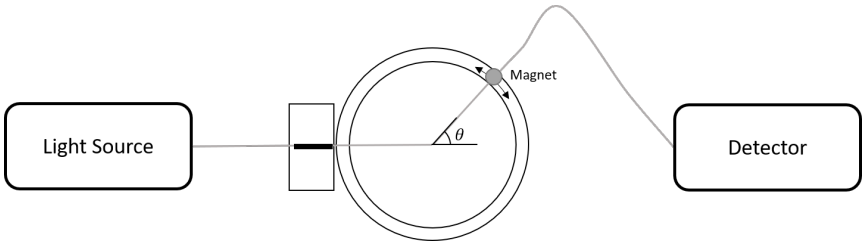

FIGURE D.1: Experimental setup for bending-loss measurements.

A simple experiment can be devised to roughly ascertain the guiding capabilities of a microfiber, through the analysis of the optical transmission of a bent microfiber (Figure D.1). The radiation from an Infrared light-source, *Photonetics FIBERWHITE* Broadband Erbium-Doped Fiber Source propagates through the microfiber and is collected by an Optical Spectrum Analyzer (*Advantest Q8384*). To actively control its curvature, the taper had one end magnetically attached to a manual rotary positioning stage, with the other end's direction being fixed by an aluminum capillary tube.

The Optical Transmission, at $\lambda = 1550$ nm, was recorded for angles θ ranging from 0° to 180° in 10° increments, for 10 μm and 5 μm microfibers (Figure D.2). There is low loss due to curvature: for $d = 10$ μm the maximum loss is less than 2%, and less than 20% for $d = 5$ μm. Higher losses occur when the radius of curvature is on the order of micrometers.

The fabricated microfibers show high transmission when bent, which is a great advantage for compact applications.

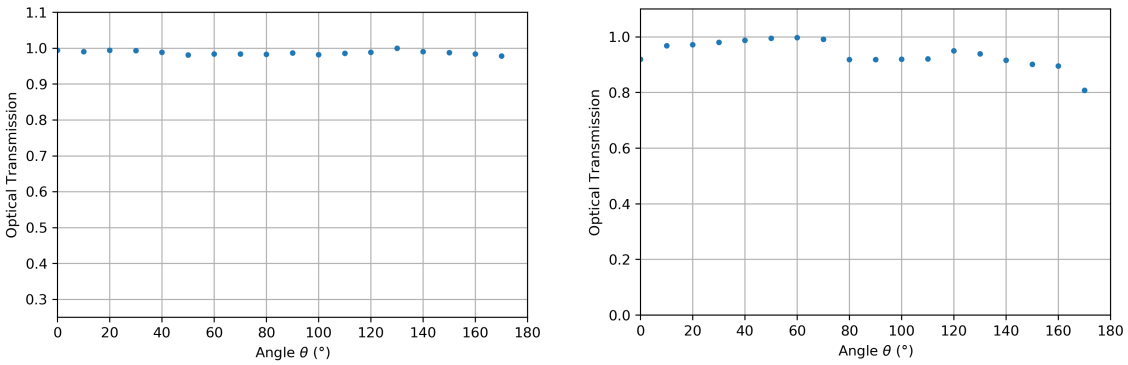

(A) $d = 10\mu$m (B) $d = 5\mu$m

FIGURE D.2: Optical Transmission dependence on the curvature for microfibers with 10μm and 5μm waist diameters.

Appendix E

Thermo-Optic Effect on Water

In water, the Cauchy equation can be modified in order to consider the temperature dependence ($n = n(\lambda, T)$) [122]:

$$n(\lambda, T) = A(T) + \frac{B(T)}{\lambda^2} + \frac{C(T)}{\lambda^4} + \frac{D(T)}{\lambda^6} \tag{E.1}$$

with the Temperature-dependent A, B, C and D coefficients:

$$\begin{aligned} A(T) &= 1.3208 - 1.2325 \cdot 10^{-5} \cdot T - 1.8674 \cdot 10^{-6} \cdot T^2 + 5.0233 \cdot 10^{-9} \cdot T^3 \\ B(T) &= 5208.2413 - 0.5179 \cdot T - 2.284 \cdot 10^{-2} \cdot T^2 + 6.9608 \cdot 10^{-5} \cdot T^3 \\ C(T) &= -2.5551 \cdot 10^{8} - 18341.336 \cdot T - 917.2319 \cdot T^2 + 2.7729 \cdot T^3 \\ D(T) &= 9.3495 + 1.7855 \cdot 10^{-3} \cdot T + 3.6733 \cdot 10^{-5} \cdot T^2 - 1.2932 \cdot 10^{-7} \cdot T^3 \end{aligned} \tag{E.2}$$

The ranges of validity are $\lambda \in [200 - 1000]$ nm and $T \in [0 - 100]$ °C.

For increasing temperature, the refractive index of water decreases, as shown in Figure E.1. For example, at 600 nm, thermo-optic coefficient is approximately 1.5×10^{-4} RIU/°C.

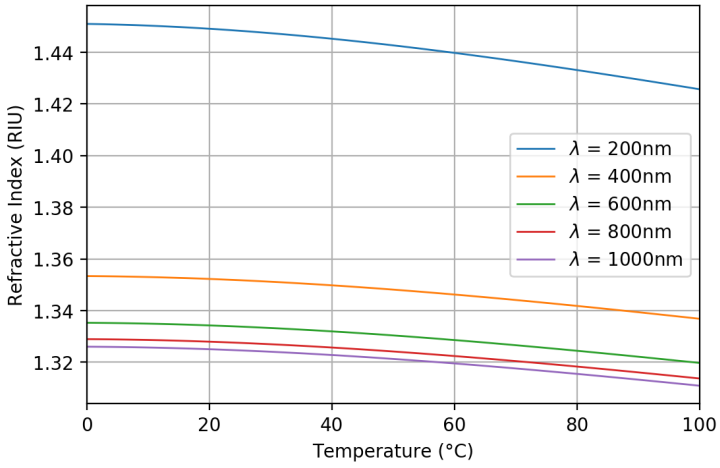

(A) Temperature dependence.

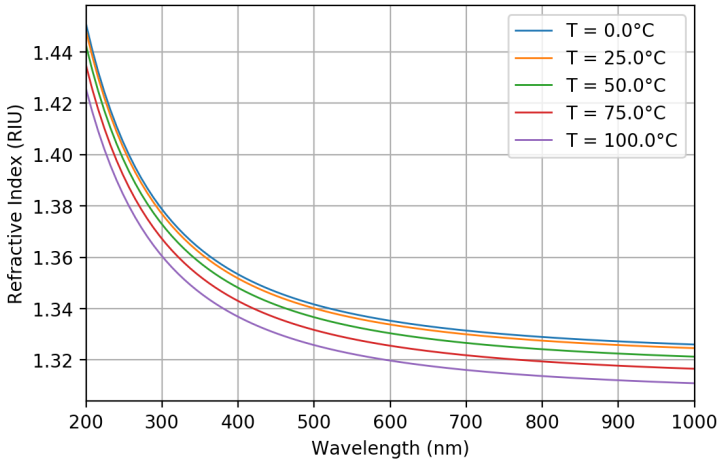

(B) Wavelength dependence.

FIGURE E.1: The Thermo-Optic Effect on Water. Dependence of the Temperature (top) and wavelength (bottom) in the refractive index.

Bibliography

[1] L. Tong, R. R. Gattass, J. B. Ashcom, S. He, J. Lou, M. Shen, I. Maxwell, and E. Mazur, "Subwavelength-diameter silica wires for low-loss optical wave guiding," *Nature*, vol. 426, no. 6968, pp. 816–819, 2003.

[2] G. Brambilla, "Optical fibre nanowires and microwires: A review," *Journal of Optics A: Pure and Applied Optics*, vol. 12, no. 4, 2010.

[3] L. Tong, "Micro/nanofibre optical sensors: Challenges and prospects," *Sensors (Switzerland)*, vol. 18, no. 3, 2018.

[4] R. Ismaeel, T. Lee, M. Ding, M. Belal, and G. Brambilla, "Optical microfiber passive components," *Laser and Photonics Reviews*, vol. 7, no. 3, pp. 350–384, 2013.

[5] G. Brambilla, "[INVITED] Optical microfibre devices," *Optics & Laser Technology*, vol. 78, pp. 76–80, 2016.

[6] G. Brambilla, F. Xu, P. Horak, Y. Jung, F. Koizumi, N. P. Sessions, E. Koukharenko, X. Feng, G. S. Murugan, J. S. Wilkinson, and D. J. Richardson, "Optical fiber nanowires and microwires: fabrication and applications," *Adv. Opt. Photon.*, vol. 1, no. 1, pp. 107–161, jan 2009.

[7] C. Rao, F. Deepak, G. Gundiah, and A. Govindaraj, "Inorganic nanowires," *Progress in Solid State Chemistry*, vol. 31, no. 1-2, pp. 5–147, 2003.

[8] T. Birks and Y. Li, "The Shape of Fiber Tapers," *Journal of Lightwave Technology*, vol. 10, no. 4, pp. 432–438, 1992.

[9] L. Tong, J. Lou, R. Gattass, S. He, X. Chen, L. Liu, and E. Mazur, "Assembly of silica nanowires on silica aerogels for microphotonic devices," *Nano Letters*, vol. 5, no. 2, pp. 259–262, 2005.

[10] F. Orucevic, V. Lefèvre-Seguin, and J. Hare, "Transmittance and near-field characterization of sub-wavelength tapered optical fibers," *Optics Express*, vol. 15, no. 21, pp. 13 624–13 629, 2007.

[11] R. Nagai and T. Aoki, "Ultra-low-loss tapered optical fibers with minimal lengths," *Optics Express*, vol. 22, no. 23, pp. 28 427–28 436, 2014.

[12] Y. Xu, W. Fang, and L. Tong, "Real-time control of micro/nanofiber waist diameter with ultrahigh accuracy and precision," *Optics Express*, vol. 25, no. 9, pp. 10 434–10 440, 2017.

[13] G. Brambilla, V. Finazzi, and D. D. J. Richardson, "Ultra-low-loss optical fiber nanotapers," *Opt. Express*, vol. 12, no. 10, pp. 2258–2263, 2004.

[14] A. Felipe, G. Espíndola, H. Kalinowski, J. Lima, and A. Paterno, "Stepwise fabrication of arbitrary fiber optic tapers," *Optics Express*, vol. 20, no. 18, pp. 19 893–19 904, 2012.

[15] J. M. Ward, A. Maimaiti, V. H. Le, and S. N. Chormaic, "Contributed review: Optical micro- and nanofiber pulling rig," 2014.

[16] J. E. Hoffman, S. Ravets, J. A. Grover, P. Solano, P. R. Kordell, J. D. Wong-Campos, L. A. Orozco, and S. L. Rolston, "Ultrahigh transmission optical nanofibers," *AIP Advances*, vol. 4, no. 6, 2014.

[17] "National center for biotechnology information. pubchem database. silicon dioxide, cid=24261,," (accessed on Aug. 29, 2019). [Online]. Available: https://pubchem.ncbi.nlm.nih.gov/compound/Silicon-dioxide

[18] G. Brambilla, F. Xu, and X. Feng, "Fabrication of optical fibre nanowires and their optical and mechanical characterisation," *Electronics Letters*, vol. 42, no. 9, pp. 517–519, 2006.

[19] L. Ding, C. Belacel, S. Ducci, G. Leo, and I. Favero, "Ultralow loss single-mode silica tapers manufactured by a microheater," *Applied Optics*, vol. 49, no. 13, pp. 2441–2445, 2010.

[20] G. Brambilla, Y. Jung, and F. Renna, "Optical fiber microwires and nanowires manufactured by modified flame brushing technique: Properties and applications," *Frontiers of Optoelectronics in China*, vol. 3, no. 1, pp. 61–66, 2010.

[21] N. Vukovic, N. Broderick, M. Petrovich, and G. Brambilla, "Novel method for the fabrication of long optical fiber tapers," *IEEE Photonics Technology Letters*, vol. 20, no. 14, pp. 1264–1266, 2008.

[22] G. Brambilla, F. Koizumi, X. Feng, and D. Richardson, "Compound-glass optical nanowires," *Electronics Letters*, vol. 41, no. 7, pp. 400–402, 2005.

[23] L. Shi, X. Chen, H. Liu, Y. Chen, Z. Ye, W. Liao, and Y. Xia, "Fabrication of submicron-diameter silica fibers using electric strip heater," *Optics Express*, vol. 14, no. 12, pp. 5055–5060, 2006.

[24] C. Baker and M. Rochette, "A generalized heat-brush approach for precise control of the waist profile in fiber tapers," *Optical Materials Express*, vol. 1, no. 6, pp. 1065–1076, 2011.

[25] H. Soørensen, E. Polzik, and J. Appel, "Heater self-calibration technique for shape prediction of fiber tapers," *Journal of Lightwave Technology*, vol. 32, no. 10, pp. 1886–1891, 2014.

[26] A. Coillet, B. Cluzel, G. Vienne, P. Grelu, and F. De Fornel, "Near-field characterization of glass microfibers on a low-index substrate," *Applied Physics B: Lasers and Optics*, vol. 101, no. 1-2, pp. 291–295, 2010.

[27] N. Vukovic, N. Broderick, M. Petrovich, and G. Brambilla, "Fabrication of metre-long fibre tapers," in *2008 Conference on Quantum Electronics and Laser Science Conference on Lasers and Electro-Optics, CLEO/QELS*, 2008.

[28] T. E. Dimmick, G. Kakarantzas, T. A. Birks, and P. S. J. Russell, "Carbon dioxide laser fabrication of fused-fiber couplers and tapers," *Applied Optics*, 1999.

[29] J. Ward, D. O'Shea, B. Shortt, M. Morrissey, K. Deasy, and S. Chormaic, "Heat-and-pull rig for fiber taper fabrication," *Review of Scientific Instruments*, vol. 77, no. 8, 2006.

[30] K. Mullaney, R. Correia, S. Staines, S. James, and R. Tatam, "Monitoring techniques for the manufacture of tapered optical fibers," *Applied Optics*, vol. 54, no. 28, pp. 8531–8536, 2015.

[31] A. Hartung, S. Brueckner, and H. Bartelt, "Limits of light guidance in optical nanofibers," *Optics Express*, vol. 18, no. 4, pp. 3754–3761, 2010.

[32] M. Fujiwara, K. Toubaru, and S. Takeuchi, "Optical transmittance degradation in tapered fibers," *Optics Express*, vol. 19, no. 9, pp. 8596–8601, 2011.

[33] H. Haddock, P. Shankar, and R. Mutharasan, "Fabrication of biconical tapered optical fibers using hydrofluoric acid," *Materials Science and Engineering B: Solid-State Materials for Advanced Technology*, vol. 97, no. 1, pp. 87–93, 2003.

[34] E. Zhang, W. Sacher, and J. Poon, "Hydrofluoric acid flow etching of low-loss subwavelength-diameter biconical fiber tapers," *Optics Express*, vol. 18, no. 21, pp. 22 593–22 598, 2010.

[35] L. Tong, L. Hu, J. Zhang, J. Qiu, Q. Yang, J. Lou, Y. Shen, J. He, and Z. Ye, "Photonic nanowires directly drawn from bulk glasses," *Optics Express*, vol. 14, no. 1, pp. 82–87, 2006.

[36] S. S. A. Harfenist, S. S. D. Cambron, E. E. W. Nelson, S. M. S. Berry, A. A. W. Isham, M. M. Crain, K. M. K. Walsh, R. R. S. Keynton, and R. W. R. Cohn, "Direct drawing of suspended filamentary micro- and nanostructures from liquid polymers," *Nano Letters*, vol. 4, no. 10, pp. 1931–1937, 2004.

[37] L. Tong, F. Zi, X. Guo, and J. Lou, "Optical microfibers and nanofibers: A tutorial," *Optics Communications*, vol. 285, no. 23, pp. 4641–4647, 2012.

[38] H. Xuan, W. Jin, and M. Zhang, "CO2 laser induced long period gratings in optical microfibers," *Optics Express*, vol. 17, no. 24, pp. 21 882–21 890, 2009.

[39] Z. Wei, Z. Song, X. Zhang, Y. Yu, and Z. Meng, "Miniature temperature sensor based on optical microfiber," *Chinese Optics Letters*, vol. 11, no. 11, 2013.

[40] H. Yang, S. Wang, X. Wang, Y. Liao, and J. Wang, "Temperature sensing in seawater based on microfiber knot resonator," *Sensors (Switzerland)*, 2014.

[41] A. Jasim, J. Faruki, M. Ismail, and H. Ahmad, "Fabrication and Characterization of Microbent Inline Microfiber Interferometer for Compact Temperature and Current Sensing Applications," *Journal of Lightwave Technology*, vol. 35, no. 11, pp. 2150–2155, 2017.

[42] W. Talataisong, R. Ismaeel, M. Beresna, and G. Brambilla, "A nano-fiber coupler thermometer," in *2017 Conference on Lasers and Electro-Optics Pacific Rim, CLEO-PR 2017*, vol. 2017-Janua, 2017, pp. 1–2.

[43] Y. Jiang, Z. Fang, Y. Du, E. Lewis, G. Farrell, and P. Wang, "Highly sensitive temperature sensor using packaged optical microfiber coupler filled with liquids," *Optics Express*, vol. 26, no. 1, pp. 356–366, 2018.

[44] M. Belal, Z. Song, Y. Jung, G. Brambilla, and T. Newson, "Optical fiber microwire current sensor," *Optics Letters*, vol. 35, no. 18, pp. 3045–3047, 2010.

[45] M. Belal, Z.-Q. Song, Y. Jung, G. Brambilla, and T. Newson, "An interferometric current sensor based on optical fiber micro wires," *Optics Express*, vol. 18, no. 19, pp. 19 951–19 956, 2010.

[46] G. Chen, T. Newson, and G. Brambilla, "Optical microfibers for fast current sensing," *Optical Fiber Technology*, vol. 19, no. 6 PART B, pp. 802–807, 2013.

[47] S. C. Yan, B. C. Zheng, J. H. Chen, F. Xu, and Y. Q. Lu, "Optical electrical current sensor utilizing a graphene-microfiber-integrated coil resonator," *Applied Physics Letters*, 2015.

[48] L. Zhang, F. Gu, J. Lou, X. Yin, and L. Tong, "Fast detection of humidity with a subwavelength-diameter fiber taper coated with gelatin film," *Optics Express*, vol. 16, no. 17, pp. 13 349–13 353, 2008.

[49] L. Bo, P. Wang, Y. Semenova, and G. Farrell, "Optical microfiber coupler based humidity sensor with a polyethylene oxide coating," *Microwave and Optical Technology Letters*, 2015.

[50] P. Polynkin, A. Polynkin, N. Peyghambarian, and M. Mansuripur, "Evanescent field-based optical fiber sensing device for measuring the refractive index of liquids in microfluidic channels," *Optics Letters*, vol. 30, no. 11, pp. 1273–1275, 2005.

[51] F. Xu, P. Horak, and G. Brambilla, "Optical microfiber coil resonator refractometric sensor," *Optics Express*, vol. 15, no. 12, pp. 7888–7893, 2007.

[52] F. Xu and G. Brambilla, "Demonstration of a refractometric sensor based on optical microfiber coil resonator," *Applied Physics Letters*, vol. 92, no. 10, 2008.

[53] Y.-H. Tai and P.-K. Wei, "Sensitive liquid refractive index sensors using tapered optical fiber tips," *Optics Letters*, 2010.

[54] W. Ji, H. Liu, S. Tjin, K. Chow, and A. Lim, "Ultrahigh sensitivity refractive index sensor based on optical microfiber," *IEEE Photonics Technology Letters*, vol. 24, no. 20, pp. 1872–1874, 2012.

[55] Y. Chen, S.-C. Yan, X. Zheng, F. Xu, and Y.-Q. Lu, "A miniature reflective micro-force sensor based on a microfiber coupler," *Optics Express*, vol. 22, no. 3, pp. 2443–2450, 2014.

[56] W. Li, Z. Hu, X. Li, W. Fang, X. Guo, L. Tong, and J. Lou, "High-sensitivity microfiber strain and force sensors," *Optics Communications*, vol. 314, pp. 28–30, 2014.

[57] S.-C. Yan, Y. Chen, C. Li, F. Xu, and Y.-Q. Lu, "Differential twin receiving fiber-optic magnetic field and electric current sensor utilizing a microfiber coupler," *Optics Express*, vol. 23, no. 7, pp. 9407–9414, 2015.

[58] Y. Zheng, X. Dong, C. Chan, P. Shum, and H. Su, "Optical fiber magnetic field sensor based on magnetic fluid and microfiber mode interferometer," *Optics Communications*, vol. 336, pp. 5–8, 2015.

[59] L. Luo, S. Pu, J. Tang, X. Zeng, and M. Lahoubi, "Highly sensitive magnetic field sensor based on microfiber coupler with magnetic fluid," *Applied Physics Letters*, vol. 106, no. 19, 2015.

[60] N.-K. Chen, Y.-H. Hsieh, and Y.-K. Lee, "Tapered fiber Mach-Zehnder interferometers for vibration and elasticity sensing applications," *Optics Express*, 2013.

[61] G. Y. Chen, G. Brambilla, and T. P. Newson, "Compact acoustic sensor based on air-backed mandrel coiled with optical microfiber," *Optics Letters*, 2013.

[62] J. Villatoro and D. Monzón-Hernández, "Fast detection of hydrogen with nano fiber tapers coated with ultra thin palladium layers," *Optics Express*, vol. 13, no. 13, pp. 5087–5092, 2005.

[63] D. Monzón-Hernández, D. Luna-Moreno, D. Escobar, and J. Villatoro, "Optical microfibers decorated with PdAu nanoparticles for fast hydrogen sensing," *Sensors and Actuators, B: Chemical*, vol. 151, no. 1, pp. 219–222, 2010.

[64] B. C. Yao, Y. Wu, A. Q. Zhang, Y. J. Rao, Z. G. Wang, Y. Cheng, Y. Gong, W. L. Zhang, Y. F. Chen, and K. S. Chiang, "Graphene enhanced evanescent field in microfiber multimode interferometer for highly sensitive gas sensing," *Optics Express*, 2014.

[65] S. Q. Wang, H. Zhao, Y. Wang, C. M. Li, Z. H. Chen, and V. Paulose, "Silver-coated near field optical scanning microscope probes fabricated by silver mirror reaction," *Applied Physics B: Lasers and Optics*, 2008.

[66] W. Liang, Y. Huang, Y. Xu, R. Lee, and A. Yariv, "Highly sensitive fiber Bragg grating refractive index sensors," *Applied Physics Letters*, vol. 86, no. 15, pp. 1–3, 2005.

[67] Y. Li and L. Tong, "Mach-Zehnder interferometers assembled with optical microfibers or nanofibers," *Optics Letters*, vol. 33, no. 4, pp. 303–305, 2008.

[68] M. Ding, P. Wang, and G. Brambilla, "A microfiber coupler tip thermometer," *Optics Express*, 2012.

[69] M. Sumetsky, Y. Dulashko, J. Fini, and A. Hale, "Optical microfiber loop resonator," *Applied Physics Letters*, vol. 86, no. 16, pp. 1–3, 2005.

[70] M. Sumetsky, Y. Dulashko, J. Fini, A. Hale, and D. DiGiovanni, "The microfiber loop resonator: Theory, experiment, and application," *Journal of Lightwave Technology*, vol. 24, no. 1, pp. 242–250, 2006.

[71] X. Jiang, L. Tong, G. Vienne, X. Guo, A. Tsao, Q. Yang, and D. Yang, "Demonstration of optical microfiber knot resonators," *Applied Physics Letters*, vol. 88, no. 22, 2006.

[72] P. Wang, L. Bo, Y. Semenova, G. Farrell, and G. Brambilla, "Optical microfibre based photonic components and their applications in label-free biosensing," *Biosensors*, vol. 5, no. 3, pp. 471–499, 2015.

[73] G. Y. Chen, "A Review of Microfiber and Nanofiber Based Optical Sensors," *The Open Optics Journal*, 2013.

[74] V. Balykin, K. Hakuta, F. Le Kien, J. Liang, and M. Morinaga, "Atom trapping and guiding with a subwavelength-diameter optical fiber," *Physical Review A - Atomic, Molecular, and Optical Physics*, vol. 70, no. 1, 2004.

[75] G. Brambilla, G. Senthil Murugan, J. Wilkinson, and D. Richardson, "Optical manipulation of microspheres along a sub wavelength optical wire," *Optics Letters*, vol. 32, no. 20, pp. 3041–3043, 2007.

[76] E. Vetsch, D. Reitz, G. Sagué, R. Schmidt, S. T. Dawkins, and A. Rauschenbeutel, "Optical interface created by laser-cooled atoms trapped in the evanescent field surrounding an optical nanofiber," *Physical Review Letters*, 2010.

[77] A. Maimaiti, V. G. Truong, M. Sergides, I. Gusachenko, and S. Nic Chormaic, "Higher order microfibre modes for dielectric particle trapping and propulsion," *Scientific Reports*, vol. 5, p. 9077, 2015.

[78] G. Brambilla and F. Xu, "Adiabatic submicrometric tapers for optical tweezers," *Electronics Letters*, 2007.

[79] H. Xin, R. Xu, and B. Li, "Optical formation and manipulation of particle and cell patterns using a tapered optical fiber," *Laser and Photonics Reviews*, vol. 7, no. 5, pp. 801–809, 2013.

[80] M. Abdul Khudus, T. Lee, T. Huang, X. Shao, P. Shum, and G. Brambilla, "Harmonic generation via $\chi 3$ intermodal phase matching in microfibers," *Fiber and Integrated Optics*, vol. 34, no. 1-2, pp. 53–65, 2015.

[81] V. Grubsky and J. Feinberg, "Phase-matched third-harmonic UV generation using low-order modes in a glass micro-fiber," *Optics Communications*, vol. 274, no. 2, pp. 447–450, 2007.

[82] T. Lee, "Nonlinear Properties of Optical Microfibres (PhD thesis)," Ph.D. dissertation, University of Southampton, 2013.

[83] T. Lee, Y. Jung, C. Codemard, M. Ding, N. Broderick, and G. Brambilla, "Broadband third harmonic generation in tapered silica fibres," *Optics Express*, vol. 20, no. 8, pp. 8503–8511, 2012.

[84] J. Levy, M. Foster, A. Gaeta, and M. Lipson, "Harmonic generation in silicon nitride ring resonators," *Optics Express*, vol. 19, no. 12, pp. 11 415–11 421, 2011.

[85] M. Abdul Khudus, R. Ismaeel, G. Brambilla, N. Broderick, and T. Lee, *Nonlinear Effects in Microfibers and Microcoil Resonators*, 2015.

[86] J. Lægsgaard, "Theory of surface second-harmonic generation in silica nanowires," *Journal of the Optical Society of America B: Optical Physics*, vol. 27, no. 7, pp. 1317–1324, 2010.

[87] U. Wiedemann, K. Karapetyan, C. Dan, D. Pritzkau, W. Alt, S. Irsen, and D. Meschede, "Measurement of submicrometre diameters of tapered optical fibres using harmonic generation," *Optics Express*, vol. 18, no. 8, pp. 7693–7704, 2010.

[88] R. R. Gattass, G. T. Svacha, L. Tong, and E. Mazur, "Supercontinuum generation in submicrometer diameter silica fibers," *Optics Express*, 2006.

[89] A. Hartung, A. Heidt, and H. Bartelt, "Nanoscale all-normal dispersion optical fibers for coherent supercontinuum generation at ultraviolet wavelengths," *Optics Express*, vol. 20, no. 13, pp. 13 777–13 788, 2012.

[90] S. Leon-Saval, T. Birks, W. Wadsworth, P. Russell, and M. Mason, "Supercontinuum generation in submicron fibre waveguides," *Optics Express*, vol. 12, no. 13, pp. 2864–2869, 2004.

[91] M. Foster, J. Dudley, B. Kibler, Q. Cao, D. Lee, R. Trebino, and A. Gaeta, "Nonlinear pulse propagation and supercontinuum generation in photonic nanowires: Experiment and simulation," *Applied Physics B: Lasers and Optics*, vol. 81, no. 2-3, pp. 363–367, 2005.

[92] G. Agrawal, *Nonlinear Fiber Optics*, 4th ed. Academic Press, 2006.

[93] M. Foster, A. Gaeta, Q. Cao, and R. Trebino, "Soliton-effect compression of supercontinuum to few-cycle durations in photonic nanowires," *Optics Express*, vol. 13, no. 18, pp. 6848–6855, 2005.

[94] G. Brambilla and D. N. Payne, "The Ultimate Strength of Glass Silica Nanowires," *NANO LETTERS*, vol. 9, no. 2, pp. 831–835, 2009.

[95] F. Xu and G. Brambilla, "Preservation of micro-optical fibers by embedding," *Japanese Journal of Applied Physics*, vol. 47, no. 8 PART 2, pp. 6675–6677, 2008.

[96] L. Xiao, M. Grogan, W. Wadsworth, R. England, and T. Birks, "Stable low-loss optical nanofibres embedded in hydrophobic aerogel," *Optics Express*, vol. 19, no. 2, pp. 764–769, 2011.

[97] L. Tong and M. Sumetsky, *Subwavelength and Nanometer Diameter Optical Fibers*. Springer-Verlag Berlin Heidelberg, 01 2010.

[98] L. Tong, J. Lou, and E. Mazur, "Single-mode guiding properties of subwavelength-diameter silica and silicon wire waveguides," *Optics Express*, vol. 12, no. 6, pp. 1025–1035, 2004.

[99] A. W. Snyder and J. D. Love, *Optical Waveguide Theory*. New York: Chapman & Hall, 1983.

[100] I. H. Malitson, "Interspecimen comparison of the refractive index of fused silica∗,†," *J. Opt. Soc. Am.*, vol. 55, no. 10, pp. 1205–1209, Oct 1965.

[101] E. Mägi, L. Fu, H. Nguyen, M. Lamont, D. Yeom, and B. Eggleton, "Enhanced Kerr nonlinearity in sub-wavelength diameter As2Se 3 chalcogenide fiber tapers," *Optics Express*, vol. 15, no. 16, pp. 10 324–10 329, 2007.

[102] "Corning smf-28e+ optical fiber." [Online]. Available: https://www.corning.com/media/worldwide/coc/documents/PI1463_07-14_English.pdf

[103] H. L. Sørensen, "Controlling the shape of subwavelength-diameter tapered optical fibers - towards a light-atom quantum interface," Master's thesis, Faculty of Science, University of Copenhagen, 2013.

[104] V. Kavungal, G. Farrell, Q. Wu, A. Kumar Mallik, and Y. Semenova, "Studies of geometrical profiling in fabricated tapered optical fibers using whispering gallery modes spectroscopy," *Optical Fiber Technology*, 2018.

[105] N. G. Kokodii and A. O. Natarova, "Optical fiber diameter measurement by the diffraction method with digital processing of the light scattering indicatrix," *Optics and Spectroscopy*, vol. 121, no. 1, pp. 103–108, 2016.

[106] M. Frawley, A. Petcu-Colan, V. Truong, and S. Nic Chormaic, "Higher order mode propagation in an optical nanofiber," *Optics Communications*, vol. 285, no. 23, pp. 4648–4654, 2012.

[107] Y. Xu, P. Lu, L. Chen, and X. Bao, "Recent developments in micro-structured fiber optic sensors," *Fibers*, vol. 5, no. 1, 2017.

[108] J.-L. Kou, M. Ding, J. Feng, Y.-Q. Lu, F. Xu, and G. Brambilla, "Microfiber-based bragg gratings for sensing applications: A review," *Sensors (Switzerland)*, vol. 12, no. 7, pp. 8861–8876, 2012.

[109] L. Gai, J. Li, and Y. Zhao, "Preparation and application of microfiber resonant ring sensors: A review," *Optics and Laser Technology*, vol. 89, pp. 126–136, 2017.

[110] W. Talataisong, R. Ismaeel, and G. Brambilla, "A review of microfiber-based temperature sensors," *Sensors (Switzerland)*, vol. 18, no. 2, 2018.

[111] J.-L. Kou, S.-J. Qiu, F. Xu, and Y.-Q. Lu, "Demonstration of a compact temperature sensor based on first-order Bragg grating in a tapered fiber probe," *Optics Express*, vol. 19, no. 19, pp. 18 452–18 457, 2011.

[112] P. Lu, L. Men, K. Sooley, and Q. Chen, "Tapered fiber Mach-Zehnder interferometer for simultaneous measurement of refractive index and temperature," *Applied Physics Letters*, 2009.

[113] Y. Wu, Y.-J. Rao, Y.-h. Chen, and Y. Gong, "Miniature fiber-optic temperature sensors based on silica/polymer microfiber knot resonators," *Optics Express*, vol. 17, no. 20, pp. 18 142–18 147, 2009.

[114] W. Wang, Y. Yu, Y. Geng, and X. Li, "Measurements of thermo-optic coefficient of standard single mode fiber in large temperature range," in *2015 International Conference on Optical Instruments and Technology: Optical Sensors and Applications*, 2015.

[115] J. C. Owens, "Optical Refractive Index of Air: Dependence on Pressure, Temperature and Composition," *Applied Optics*, 1967.

[116] Y. Xue, Y.-S. Yu, R. Yang, C. Wang, C. Chen, J.-C. Guo, X.-Y. Zhang, C.-C. Zhu, and H.-B. Sun, "Ultrasensitive temperature sensor based on an isopropanol-sealed optical microfiber taper," *Optics Letters*, 2013.

[117] S. Zhu, F. Pang, J. Wen, Z. Zhao, and T. Wang, "Temperature sensor based on a tapered optical fiber with ALD Nanofilm," in *Proceedings of SPIE - The International Society for Optical Engineering*, vol. 9634, 2015.

[118] S.-C. Yan and F. Xu, "A review on optical microfibers in fluidic applications," *Journal of Micromechanics and Microengineering*, vol. 27, no. 9, 2017.

[119] S. Holleis, T. Hoinkes, C. Wuttke, P. Schneeweiss, and A. Rauschenbeutel, "Experimental stress-strain analysis of tapered silica optical fibers with nanofiber waist," *Applied Physics Letters*, vol. 104, no. 16, 2014.

[120] J. C. Shin, W. G. Kwak, and Y.-G. Han, "Temperature-insensitive microfiber Mach-Zehnder interferometer for absolute strain measurement," *Journal of Lightwave Technology*, vol. 34, no. 19, pp. 4579–4583, 2016.

[121] J. Love, W. Henry, W. Stewart, R. Black, S. Lacroix, and F. Gonthier, "Tapered single-mode fibres and devices. Part 1: Adiabaticity criteria," *IEE Proceedings J Optoelectronics*, vol. 138, no. 5, pp. 343–354, 1991.

[122] A. N. Bashkatov and E. A. Genina, "Water refractive index in dependence on temperature and wavelength: a simple approximation," V. V. Tuchin, Ed., 2003, pp. 393–395.